Synergistic Interdecadal Effects of the North Pacific and North Atlantic SST on Precipitation over eastern China as revealed in the ECHAM5 simulations

Minmin Wu
Nanjing University of Information Science and Technology School of Atmospheric Sciences
Rong-Hua Zhang (rzhang@nuist.edu.cn)
Nanjing University of Information Science and Technology School of Marine Sciences
https://orcid.org/0000-0002-3332-7849
Hai Zhi
Nanjing University of Information Science and Technology School of Atmospheric Sciences
Junya Hu
Institute of Oceanology Chinese Academy of Sciences Key Laboratory of Ocean Circulation and Waves

Research Article

Keywords: Precipitation over eastern China, MTM-SVD method, Interdecadal variation, Sea surface temperature (SST), ECHAM5 simulations

Posted Date: December 20th, 2023

DOI: https://doi.org/10.21203/rs.3.rs-3709410/v1

Synergistic Interdecadal Effects of the North Pacific and North Atlantic SST on Precipitation over eastern China as revealed in the ECHAM5 simulations

Minmin Wu [1], Rong-Hua Zhang [2, 3*], Hai Zhi [1], Junya Hu[3, 4]

[1] School of Atmospheric Sciences, Nanjing University of Information Science and Technology, Nanjing 210044, China

[2] School of Marine Sciences, Nanjing University of Information Science and Technology, Nanjing 210044, China

[3] Laoshan Laboratory, Qingdao 266237, China

[4] Key Laboratory of Ocean Circulation and Waves, Institute of Oceanology, Chinese Academy of Sciences, Qingdao 266071, China

[*]**Corresponding author email:**

Rong-Hua Zhang; rzhang@nuist.edu.cn

ABSTRACT

In this investigation, we examine the individual and synergistic effects of sea surface temperature (SST) in the North Pacific and North Atlantic on precipitation interdecadal variations over eastern China using the Multi-Taper Method-Singular Value Decomposition (MTM-SVD) method based on the European Center Hamburg model version 5 (ECHAM5) simulations. Results reveal that the model adequately reproduces the quasi-periodic precipitation responses corresponding to interdecadal SST forcing in the North Pacific, North Atlantic and both regions. The Pacific Decadal Oscillation (PDO) is closely related to a meridional tri-polar precipitation pattern over eastern China. This precipitation pattern is attributed to the western Pacific subtropical high and surface pressure anomalies over northern East Asia, influenced by the joint effects of a mid-latitude wave train and SST anomalies in the central-western North Pacific. The North Atlantic basin-scale SST (NABS) correlates positively with precipitation over North China and negatively with precipitation over Southwest China. This precipitation pattern is affected by the westward shift of the atmospheric activity center over East Asia associated with the mid-latitude wave train across Eurasia. The combined SST forcing from the North Pacific and North Atlantic results in a meridional precipitation dipole pattern, and partially explains the precipitation interdecadal variation as observed. That is, as the PDO warm phase transitions to the NABS warm phase, rainbands experience an interdecadal northward shift from South China to North China. These results are pivotal for understanding how interdecadal SST forcing in the North Pacific and North Atlantic influences the

precipitation distribution over China, thereby contributing to improvements in interdecadal climate prediction.

Keywords: Precipitation over eastern China; MTM-SVD method; Interdecadal variation; Sea surface temperature (SST); ECHAM5 simulations

1. Introduction

Precipitation anomalies over China, particularly the corresponding extreme events, can cause droughts, floods and secondary disasters, posing significant hazards to human life, regional agriculture, economy and society (Hu et al., 2020). For example, the severe summer drought in Henan Province in 2014 (Wang et al., 2018) and the record-breaking Meiyu event over the Yangtze River basin in 2020 (e.g., Qiao et al., 2021; Zhou et al., 2021) seriously threatened local living conditions. Various studies have highlighted the impacts of multi-timescale sea surface temperature (SST) forcing on precipitation over China through different mechanisms, such as the El Niño-Southern Oscillation (ENSO; Zhi et al., 2012; Chen et al., 2013; Zhang and Gao, 2016; Gao et al., 2022; Hu et al., 2023), Pacific Decadal Oscillation (PDO; Zhang et al., 1998; Zhou et al., 2014; Zhang et al., 2016a), and Atlantic Multidecadal Oscillation (Wang et al., 2009; Si and Ding, 2016; Ding et al., 2020b). Hence, understanding the synergistic evolution between the low-frequency variability in precipitation over China and multi-timescale SST forcing in different oceans is of great significance for improving precipitation prediction, disaster prevention and reduction in China.

Previous studies have identified multiple temporal signals in precipitation over China, including seasonal, interannual, interdecadal, and multi-decadal variabilities (e.g., Lau and Li, 1984; Qian and Zhou, 2014; Ding et al., 2020a; Wu et al., 2023). Interdecadal variabilities, as an essential source of multi-time scale variations, provide a climatic background on which interannual variations evolve in precipitation and SST. For example, on the interdecadal and longer time scales, precipitation variations over China exhibit diverse dominant cycles and spatial patterns (e.g., Ding et al., 2008; Du et al., 2022; Wu et al., 2023). The summer precipitation over eastern China displays several interdecadal scales with 12 years, 30–40 years and 80 years (Ding et al., 2008). In particular, Meiyu precipitation exhibits interdecadal variations with 12–16 years, quasi-32 years, and quasi-64 years (Liang et al., 2018). Furthermore, interdecadal variability in summer precipitation over China show spatial patterns with a regime transition of meridional mode from a tri-pole pattern to a dipole pattern (Ding et al., 2008). Li et al. (2018) pointed out two interdecadal modes of summer precipitation in South China: an in-phase mode across the region and an anti-phase mode in the east and west, respectively. However, spatial patterns and their evolutions of precipitation variability over China at specific interdecadal scales are still not well characterized.

In terms of the interdecadal variations in precipitation over China, SST anomalies in the North Pacific and North Atlantic have been regarded as important modulators (e.g., Lyu et al., 2014; Zhu et al., 2015; Li et al., 2019; Liu et al., 2019; Wu and Wang, 2019; Zhang et al., 2022a). The PDO, as an interdecadal SST mode in the North

Pacific, can regulate the precipitation over China through the related water vapor transport associated with the north-south motion of the East Asian monsoon (Zhang et al., 2018) and the intensity and position of western Pacific subtropical high (WPSH) and western North Pacific anomalous anticyclone (Chang et al., 2000; Li et al., 2014; Dong, 2016; Zhang et al., 2016b; Zhang et al., 2017). Furthermore, oceanic forcing in the North Atlantic has been found to affect precipitation over East Asia through various pathways (e.g., Li et al., 2013; Li et al., 2019; Liu et al., 2020; Chen et al., 2022). The North Atlantic SST anomaly can affect precipitation over China by triggering a mid-high latitude teleconnection wave train and a Gill-Matsuno-type response in the tropical western Pacific (Wu et al., 2009; Wu et al., 2012). Additionally, tropical North Atlantic warming in spring can induce a trans-tropical climate response, which can transport water vapor to central China through the western North Pacific anticyclone (Chen et al., 2022).

These studies primarily focused on the relationships of single regional SST forcing with precipitation variations over China, as well as the associated processes (e.g., Li et al., 2013; Lyu et al., 2014; Zhu et al., 2015; Li et al., 2019; Liu et al., 2019; Wu and Wang, 2019; Liu et al., 2020; Chen et al., 2022). Recent attention has paid to the combined effects of the SST in the North Pacific and North Atlantic on precipitation over China (e.g., Zhu et al., 2015; Li et al., 2018; Zhang et al., 2018). Due to the complexity of precipitation variabilities affected by different climate modes, signals with interannual-to-interdecadal SST forcing from multiple basins and precipitation responses over China are superimposed and mixed together, making it challenging to isolate cause-effect relationships effectively. There are still uncertainties in assessing the relative contributions of SST forcing in the North Pacific and North Atlantic to interdecadal variations in precipitation over China from observations. There is a clear need to clarify precipitation responses to SST forcing in the North Pacific or North Atlantic at specific cycles based on model sensitivity experiments (Zhang et al., 2020; Zhang et al., 2022b; Hu et al., 2023). Further efforts aim to demonstrate corresponding dynamic processes and physical mechanisms through the co-varying SST, precipitation and associated atmospheric circulation fields.

To this end, the Atmospheric General Circulation Model of European Center Hamburg model version 5 (ECHAM5; Roeckner et al., 2003) is used in this study for the focused analyses of precipitation responses over China to interdecadal SST forcing in the North Pacific, North Atlantic and both regions. The Multi-Taper Method (MTM)–Singular Value Decomposition (SVD) is performed to separate dominant temporal cycle signals from coupled climate fields (including precipitation, SST and associated atmospheric fields) and then reconstruct their spatiotemporal patterns at a specific interdecadal cycle (Mann and Park, 1994; Tourre et al., 1999; Wei et al., 2013). Thus, relevant processes and mechanisms can be identified by the co-varying coupled fields reconstructed at corresponding cycles. We aim to understand the individual and synergistic effects of SST forcing in the North Pacific and North Atlantic on precipitation variations over China on the interdecadal times scale.

The remainder of this paper is structured as follows. Section 2 introduces the data, model and methods used in this study. Section 3 delineates the dominant interdecadal cycles of the simulated precipitation driven by SST forcing in different regions in the ECHAM5. Section 4 describes the interdecadal co-varying characteristics of the North Pacific SST, simulated precipitation over China and related atmosphere circulations, and analyzes the related processes and potential mechanisms. Section 5 replicates the analyses for the North Atlantic SST. Section 6 assesses the synergistic effects of the SST in the North Pacific and North Atlantic on the interdecadal precipitation variations. The main conclusions and discussions are presented in section 7.

2 Data and methods

2.1 Data

Monthly precipitation data used in this research are obtained from the Climatic Research Unit (CRU) at the University of East Anglia, based on observations from global meteorological stations, with a spatial resolution of 0.5°×0.5° (Harris et al., 2020). Monthly SST data are obtained from the Hadley Center Sea Ice and Sea Surface Temperature dataset version 1.1 (HadISST v1.1), with a horizontal resolution of 1°×1° (Rayner et al., 2003). The climatic mean of SST fields used in the model simulations is derived from the Atmospheric Model Intercomparison Project II Sea Surface Temperature and Sea Ice Concentration Boundary Conditions. The datasets utilized in this study cover the period from 1951 to 2020 (840 months), and the climatological mean is defined as the average during 1971–2010.

2.2 Multi-Taper Method–Singular Value Decomposition

The MTM–SVD method is adopted to detect and reconstruct climate signals on various timescales (Mann and Park, 1994). This method is capable of tracking the evolution characteristics of two or more coupled climate fields (i.e. SST, pressure and precipitation fields) at varying timescales (Mann and Park, 1994; Tourre et al., 1999; Wei et al., 2013). Initially, the MTM–SVD method is employed to transform climate fields (a single field or combined multiple fields) into a spectral domain through the MTM process (Thomson, 1982). Subsequently, the SVD is applied to identify significant patterns of spatiotemporal variabilities.

The MTM–SVD decomposes a multivariate dataset of *M* spatially distributed time series into *K* orthogonal modes at frequency *f*, expressed as Eq. (1).

$$A(f)=\begin{bmatrix} Y_1^1 & Y_2^1 & \cdots & Y_K^1 \\ Y_1^2 & Y_2^2 & \cdots & Y_K^2 \\ \cdots & \cdots & \cdots & \cdots \\ Y_1^M & Y_2^M & \cdots & Y_K^M \end{bmatrix} = \sum_{k=1}^{K} U_k(f)\gamma_k(f)V_k \qquad (1),$$

where $\gamma_k(f)$ represents the singular value, describing the relative amplitude for each among the *K* orthogonal modes. The left singular vector, $U_k(f)$, is the spatial Empirical Orthogonal Function (EOF) mode, encapsulating the spatial amplitude and phase information of that mode. The right singular vector, V_k, denotes the spectral EOF, describing the relative combination of *K* independent data tapers that characterizes the temporal modulation envelope of oscillation signals. Y indicates the Fourier spectral estimate for the mth time series x (appropriately normalized) corresponding to the kth orthogonal data taper, a_k^m,

$$Y_k^m(f) = \sum_{n=1}^{N} a_k^m(t) x^m(t) e^{i2\pi f n\Delta t} \qquad (2),$$

where $n\Delta t$ is the sample interval (e.g., monthly, seasonal, annual).

The Local Fractional Variance (LFV) spectrum, $\gamma_1^2(f)/\sum_{k=1}^{K}\gamma_k^2(f)$, provides an effective parameter for frequency-domain signal detection, where peaks indicate potentially significant spatiotemporal signal at that frequency. Statistical confidence levels of the significance test for the LFV spectrum are estimated by using the bootstrap method (Mann and Park, 1999).

If a significant spatiotemporal signal centered at frequency f_0 is detected, we can reconstruct the spatiotemporal signals by the following.

$$\tilde{x}_n^m(t) = \delta(f_0)\Re\left\{\sigma^m U_1^m(f_0)\alpha_1(n\Delta t)e^{-i2\pi f_0 n\Delta t}\right\} \qquad (3),$$
$$\alpha_1(n\Delta t) = \sum_{k=1}^{K} \xi_k^{-1}\gamma_k(f_0)V_k^1 a_k$$

where the variable amplitude $\alpha_1(n\Delta t)$ represents the slowly varying temporal envelope of the oscillation signal at frequency f_0, which can be obtained by constructing a linear combination of Slepian data tapers and the kth component of the first mode spectral EOF (V_k^1). The term ξ_k^{-1} indicates the bandwidth retention factors of the orthogonal data tapers.

2.3 Model overview and sensitivity experiment design

Figure 1a shows the LFV spectrum of observed precipitation over China. There is a significant interdecadal peak at 24.4-year. We will focus on this interdecadal signal for its relationship with SST forcing in the North Pacific and North Atlantic using an atmospheric model. This investigation adopts the Atmospheric General Circulation Model of the ECHAM5 (Roeckner et al., 2003), which has 17 vertical layers and a horizontal resolution of 1.85°×1.85°. The integration time of the ECHAM5 is from 1951 to 2020 (70 years or 840 months in total), and monthly field are outputs for analyses. The SST forcing field of the model is a time-varying interdecadal SST signal (with a 24.4-year cycle) extracted from the observations through the MTM–SVD; the same signal can also be identified from the LFV spectrum of observed precipitation over China (Fig. 1a). In the ECHAM5 simulations, the time-varying interdecadal SST forcing fields are used to simulate precipitation response, which is reconstructed by superimposing the regional interdecadal SST anomaly signal on the climatological mean of SST fields.

The reconstructed evolution patterns of the SST anomalies in the North Pacific show similarities with that of the PDO (Mantua et al., 1997; Zhang and Levitus, 1997), exhibiting an anti-phase variation between the central North Pacific (CNP) and the west coast of North America-tropical eastern Pacific (Fig. 1b). The pattern correlation coefficient is 0.82 between the reconstructed distribution of the North Pacific SST and the canonical PDO pattern. In the North Atlantic, the reconstructed evolution pattern of the SST anomalies displays an Atlantic Multidecadal Oscillation-like pattern, with an in-phase variation in large-scale basin SST anomalies, i.e., North Atlantic basin-scale SST (NABS) mode. On a 24-year cycle, the variations in the mature phases of the PDO and NABS are temporally inconsistent (Fig. 1c).

In order to investigate the interdecadal response of precipitation over China to PDO and NABS patterns, sensitivity experiments with different interdecadal SST forcing fields are designed, as shown in Table 1. The control experiment (CTL experiment) is forced by the climatological mean of SST fields with seasonal variations. The forcing fields for the North Pacific (PAC experiment) and North Atlantic interdecadal SST experiment (ATL experiment) are obtained by superimposing corresponding regional interdecadal SST anomalies on the climatological mean of SST fields. Considering that the simulated atmospheric response is generally weak, the superimposed SST interdecadal anomaly amplitude is rescaled to be four times as large as the extracted values. To obtain the responses of precipitation and related atmospheric circulation fields to interdecadal SST forcing in different regions, we subtract the results of the control experiment from those of the corresponding sensitivity experiments.

In this study, we calculate the reconstructed PDO and NABS indexes according to SST variability center. The PDO index is defined as the normalized time series of the reconstructed SST averaged over the CNP (170°E–150° W, 28°N–45°N) and then is multiplied by a coefficient of −1 to ensure the consistency of the signal variation in the PDO phase with the observations. The NABS index is defined as the normalized time series of the reconstructed SST averaged over the domain of 80°W–0°, 20°–65°N. The threshold with a 1-time standard deviation is applied to select the positive and negative phases of the PDO and NABS for composite analyses. The student t-test is used to perform a significance test for the composite analyses at different statistical confidence levels.

3. Dominant cycles of the simulated precipitation

We first demonstrate that the ECHAM5 can capture the corresponding periodic variations in precipitation over China under the interdecadal SST forcing (with a 24.38-year cycle). Figure 2 presents the time series and their wavelet analyses of the simulated precipitation signals over the subregions of China under different simulation conditions. Notably, the simulated precipitation signals over North China, the middle and lower reaches of the Yangtze River (MLYR), and South China exhibit prominent peaks in the spectral range of 20–35 years, which are significant at the 90% confidence level (Figs. 2d–2f). In the PAC experiment (Figs. 2d), the significant interdecadal peaks of the simulated precipitation over North China, the MLYR, and South China are seen at 32-year, 32-year, and 24-year, respectively. The variance of precipitation signals is the largest in the MLYR, followed by South China, and smallest in North China. In the ATL experiment (Figs. 2e), the significant interdecadal peaks of the simulated precipitation over North China, the MLYR, and South China are seen at 32-year, 24-year, and 24-year, respectively. The variance of precipitation signals is the largest in North China, followed by South China, and smallest in the MLYR. Under the joint effects of the interdecadal SST forcing in the combined North Pacific and North Atlantic (CPA experiment, as shown in Figs. 2f), the significant interdecadal peaks of simulated precipitation over North China, the MLYR, and South China are all seen at the 32-year. The variance of precipitation signals is the largest in

North China, followed by South China, and lowest in MLYR. These results indicate that the cycles of the simulated precipitation are close to those of precipitation and SST in the observations (Fig. 1a), albeit with a frequency shift in the simulations.

The simulated precipitation cycles align with the cycles of the SST forcing fields, implying that the ECHAM5 model can simulate the corresponding periodic response of precipitation over China under interdecadal SST forcing in different regions. This motivates us to further investigate the co-varying characteristics of the precipitation and SST on an interdecadal scale and evaluate the synergistic effects of the North Pacific and North Atlantic SST on interdecadal precipitation variations over China. Thus, we reconstruct the combined fields (including the simulated precipitation over China, sea level pressure, 850-hPa winds, 500-hPa geopotential height, vertically integrated water vapor flux and its divergence, and the corresponding SST forcing fields) with a 24.38-year cycle around the center of the SST forcing cycle. Based on this, we can obtain the co-varying characteristics of the SST, precipitation and associated atmospheric circulation fields simulated by the PAC, ATL and CPA experiments, respectively. Since the calculations are based on a narrow frequency band, the reconstructed amplitudes of the precipitation and atmospheric circulations are relatively small. It should be noted that the amplitude of the reconstructed SST anomalies increases dramatically due to the coincidence of the reconstruction cycle with the SST field cycle. Considering that the observed precipitation variation over Northwest China is trivial on the 23-year cycle (its standard deviation is less than 1 mm mon^{-1}) as reported by Wu et al. (2023), we put our attention to the precipitation over eastern China (90°–135°E, 20°–55°N) in the following analysis.

4. North Pacific interdecadal SST experiment (PAC experiment)

In the PAC experiment, the interdecadal SST in the North Pacific is associated with the PDO (Fig. 1b), which is used to drive the model for numerical integration. The following analyses focus on characterizing the precipitation response over eastern China when the CNP shows warm SST anomalies (i.e., PDO cold phase, PDO−) and analyzing the possible processes and mechanisms involved.

4.1 Interdecadal pattern of precipitation over China

Under the influence of the PDO, the simulated precipitation anomalies over China exhibit a meridional tri-pole pattern, with the precipitation centers located in South China, MLYR and North China (Figs. 3 a). The polarity of this tri-pole precipitation pattern shifts with the phase of the SST anomalies in the CNP (Figs. 3 b). The precipitation anomalies over China display a meridional "− + −" distribution during the PDO warm phase (PDO+). When the CNP is colder during 1952–1961, 1976–1998 and 2013–2020, the precipitation increases over the MLYR but decreases over North China and South China. A similar situation with opposite polarity appears during 1961–1976 and 1999–2013, respectively.

The reconstructed PDO index turns from negative to positive in 1976 and then to negative after 2000 (Fig. 3 c), consistent with the previous work (Qian and Zhou, 2014), indicating its capability to reflect PDO variations. The variations in precipitation patterns match well with the variations in the PDO index. The variations in precipitation patterns coincide well with the variations in the PDO index. Selecting the mature stages of the PDO (Table 2) for the composited analysis of the simulated precipitation and North Pacific SST further suggests that a meridional tri-polar precipitation pattern with the "− + −" distribution is favored by the PDO+ (Figs. 3d and 3e), and vice versa.

4.2 Synergistic evolution characteristics of precipitation and SST

In order to analyze the synergistic evolution of the SST, precipitation and associated atmospheric circulation fields at different stages of the PDO−, we artificially set phase 0° as the situation when a warm center appears in the CNP. Figure 4 illustrates the half-cycle evolutions of precipitation over China and SST in the North Pacific. During the first 1/4 cycle (phases 0°–60°), the North Pacific SST exhibits warming in the CNP and cooling in the west coast of North America-tropical eastern Pacific, corresponding to the development stages of the PDO−. Therefore, the North Pacific SST distribution during the post 1/4 cycle (phases 90°–150°) corresponds to the decaying stages of the PDO−.

During the PDO+ mature stages (phases 30°–90), the evolution of the simulated precipitation anomalies exhibits large amplitudes in South China, the MLYR, and North China, as shown in Figure 4 a. The precipitation anomaly amplitude in the centers from south to north reach up to 10, 15 and 15 mm mon^{-1}, respectively. When a warm center appears in the CNP at phase 0°, the precipitation anomaly distribution over China shows a meridional "+ − +" tri-polar pattern, with positive anomalies over South China and North China and negative anomalies over the MLYR. Accompanied by the enhanced CNP warming and California-equatorial Pacific surface cooling during the development stage of the PDO− (phases 0°–60°), the meridional tri-polar pattern of precipitation anomalies is enhanced. This meridional tri-polar pattern weakens during the decaying stages of the PDO− (phases 90°–150°) with the decays of the CNP warming and North American west coast cooling.

Overall, the simulated precipitation anomalies over China show a meridional tri-pole pattern under the forcing of the PDO-related SST in the North Pacific. During the PDO− phase, the precipitation increases over the MLYR and decreases over North China and South China, and vice versa for the PDO+ phase. When the PDO− develops (decays), the tri-pole pattern of precipitation anomalies strengthens (weakens).

4.3 The influence mechanisms

How does the atmospheric response to the PDO further contribute to the meridional tri-pole pattern of precipitation over China? We perform further analyses in the subsection.

a. Local and remote atmospheric responses to the PDO

North Pacific SST anomalies can directly affect both local and global atmospheric circulations during the PDO−. During the development stage of the PDO− (Figs. 4 a–c), concurrent with the enhanced warming in the CNP and cooling in the Aleutian-Eastern Pacific, low-pressure anomalies over the central-western Pacific weaken, and high-pressure anomalies over the Aleutian-Eastern Pacific intensify. This anomalous high pressure over the Aleutian weakens the Aleutian Low (AL). As the CNP warming decays and the cold SST anomalies expand westward to the whole North Pacific during the decaying stage of the PDO− (Figs. 4 d–f), the low-pressure anomalies retreat to the western Pacific, and the high-pressure anomalies expand to cover almost the whole North Pacific. The variations of low-pressure anomalies over the western Pacific can be associated with the WPSH variations.

The influences of the North Pacific SST extends beyond the local region, impacting the East Asian atmosphere through a teleconnection wave train across Eurasia (Fig. 5). The 500-hPa geopotential height reveals a mid-latitude wave train propagating from the North Atlantic to northern East Asia, and its activity centers are located in the Arctic, North Sea, Caspian Sea, Lake Baikal, and the Sea of Okhotsk-western Pacific (Figs. 5 b–e). In the East Asia, the atmospheric activity center corresponding to an anomalous high pressure shows a noticeable northwestward shift during the PDO−, with its intensity strengthening during the first 1/4 cycle and weakening during the latter 1/4 cycle (Figs. 6 a–f). Concurrently, pressure anomalies over the western Pacific experience a transition from positive to negative. Specifically, negative geopotential height anomalies prevail over the western Pacific north of 25°N during phases 60°–120°, indicating that the WPSH is weak throughout much of the PDO−. These findings highlight the coexistence of an anomalous high-pressure center over Northeast China and a weak WPSH during the mature stage of the PDO− (phases 60°–90°).

Different atmospheric processes associated with the PDO can lead to a weak

WPSH and anomalous high pressure over northern East Asia. On the one hand, the western Pacific warming throughout the PDO− phase can enhance local convective activities (Zhang et al., 2016b), consequently weakening the WPSH. On the other hand, the mid-latitude wave train not only promotes the emergence of anomalous high pressure over northern East Asia but also induces anomalous upward motion in the western Pacific, further contributing to the weakening of the WPSH. Therefore, high-pressure anomalies over northern East Asia may be predominantly influenced by the wave train across Eurasia, while the weak-than-normal WPSH is the result of the joint effects of the mid-latitude wave train and local warm SST anomalies.

b. Influences of East Asia atmospheric circulations on precipitation

The anomalous high pressure over northern East Asia and the weak WPSH jointly dominate the atmospheric circulation and water vapor transport over East Asia during the PDO− (Fig. 6). Evidently, an anomalous anticyclone strengthens and shifts northwestward in tandem with the variations of local high-pressure anomalies. These accompanying southerly wind anomalies facilitate increased northward water vapor transport to North China (Figs. 6a–f), leading to enhanced local precipitation (Figs. 6g–l). Simultaneously, in the western Pacific, the anomalous cyclone associated with the weak WPSH induces northerly wind anomalies south of the MLYR, hindering the northward transport of warm and moist water vapor originating from the South China Sea. This results in notable water vapor flux divergence over the south of MLYR, which inhibits the occurrence of local precipitation. Thus, the variations in water vapor conditions, accompanied by East Asian circulation anomalies during the PDO−

phase, directly contribute to the “+ − +” distribution of precipitation anomalies over China.

Figure 7 presents the possible processes and potential influence mechanisms through which the PDO-related North Pacific SST anomalies cause the tri-polar pattern of precipitation anomalies over China in the PAC experiment. During the PDO− phase, the cold SST anomalies along the North American coast directly induce high-pressure anomalies, weakening the AL. This atmospheric response can impact the North Atlantic Oscillation (NAO) in the North Atlantic through a “see-saw” change between the AL and Iceland Low (Honda et al., 2001; Dong et al., 2014) and further trigger a mid-latitude wave train across Eurasia (Li et al., 2013). Correspondingly, the high-pressure anomalies over northern East Asia result in local descending motion. Moreover, the warm SST anomalies in the central-western North Pacific enhance local convection. The enhanced local convection and mid-latitude wave train can jointly weaken the WPSH. As a result, the combined effects of the high-pressure anomalies over northern East Asia and weak WPSH lead to northerly wind anomalies prevailing south of the MLYR and southerly wind anomalies prevailing over North China. The former is conducive to increased precipitation over North China due to the local convergence of water vapor. The latter not only impedes water vapor transport to North China, but also causes water vapor divergence over the MLYR, weakening local precipitation. Therefore, the modulation of local water vapor through the East Asian atmospheric circulation configuration is the primary factor contributing to the “+ − +” meridional tri-pole pattern of precipitation over China during the PDO−.

5. North Atlantic interdecadal SST experiment (ATL experiment)

5.1 Interdecadal pattern of precipitation over China

In the ATL experiment, the SST forcing for simulating periodic precipitation responses over China is associated with the NABS. As shown in Figure 8, the simulated precipitation exhibits in-phase variations from South China to North China. Positive precipitation anomalies prevail over most of eastern China during periods (1954–1968 and 1984–2006) when there exist warm SST anomalies in the North Atlantic, while the opposite occurs during cold SST anomaly periods (1969–1983 and 2007–2002). The NABS index turns from negative to positive around 1956 and 1983 and from positive to negative around 1968 and 2007 (Fig. 8c), aligning with the phases of precipitation anomalies.

Composite analyses focusing on the mature stages of the NABS (Table 3) reveal the patterns of the North Atlantic SST and the precipitation over China associated with the NABS+. During the NABS+, significant warm SST anomalies span almost the entire North Atlantic, with a warming center (>1.2°C) located north of 30°N. The cold SST anomalies only appear near the North American east coast (Fig. 8e). Correspondingly, significant positive precipitation anomalies appear from Northwest China to the Shandong Peninsula, weak positive precipitation anomalies can be found over South China and significant negative precipitation anomalies over Southwest China (Fig. 8d). These findings underscore the positive correlation of the North

Atlantic SST with precipitation over North China and the negative correlation with precipitation over Southwest China. Warming in the North Atlantic leads to a precipitation increase over North China and a precipitation decrease over Southwest China, and vice versa for cooling in the North Atlantic.

5.2 Synergistic evolution characteristics of precipitation and SST

To characterize the co-varying precipitation and SST, we further depict their half-cycle evolution. Phase 0° is defined artificially as the onset of the warm SST anomalies in the subpolar North Atlantic. The first 1/4 cycle (phases 0°–60°) represents the responses of the simulated precipitation and atmospheric circulation fields to the North Atlantic SST anomalies associated with the NABS+ development stage. The post 1/4 cycle (phases 90°–150°) reflects those associated with the NABS+ decaying stage. Phases 60°–90° correspond to the NABS+ mature stage.

Figure 9 illustrates the half-cycle evolution of the simulated precipitation and SST field associated with the NABS+ interdecadal forcing. There are two variability centers with the simulated precipitation located over North China and Southwest China, respectively. Notably, there is a discernible drought center over Southwest China, which tends to intensify and expand northeastward during the development-mature-decaying stages of the NABS+. Simultaneously, positive precipitation anomalies over North China weaken and contract. During the development stage of the NABS+ (phases 0°–60°), when the warm anomalies in the central North Atlantic expand across the basin, precipitation anomalies increase over North China and decrease over Southwest China. During the NABS+ mature stage (phases 60°–90°), positive precipitation anomalies mainly appear over North China and South China, and negative precipitation anomalies prevail over Southwest China. As the NABS+ decays (phases 90°–150°), the cold SST anomalies along North America intensify and expand eastward to western Europe. The drought center over Southwest China moves northward, and negative precipitation anomalies prevail over almost the entire eastern China region.

These results highlight a close correlation between the North Atlantic SST associated with the NABS and the simulated precipitation over North China and Southwest China. Specifically, the NABS is positively correlated with the precipitation over North China and negatively correlated with the precipitation over Southwest China. Particularly, a drought center over Southwest China enhances and moves northeastward throughout the NABS+. During the mature stage of the NABS+, precipitation increases over North China and South China and decreases over Southwest China, respectively.

5.3 The influence mechanisms

The North Atlantic SST anomalies exert a significant impact on local and global atmospheric circulations. For example, in the Azores region, low-pressure anomalies strengthen and expand in phases 0°–60°, and weaken and shrink in phases 90°–150°, with the maximum intensity appearing in phases 60°–90° (Fig. 9). This suggests that the Azores High is weaker than the climatological average during the NABS+, which may be the response to enhanced local convective activities due to the large-scale warm SST anomalies in the North Atlantic. In addition, high-pressure anomalies near

Iceland-western Europe indicate the Iceland Low weaker than the normal. The anti-phase variations in the Azores High and Iceland Low are similar to those of the NAO−. The NAO may trigger a mid-latitude wave train propagating eastward from the North Atlantic to East Asia, further affecting atmospheric circulations over East Asia (Li et al., 2013).

As depicted in the 500-hPa geopotential height fields (Fig. 10), there is a zonal wave train across Eurasia during the NABS+, with its activity centers located in the Azores, Kazakhstan, Lake Baikal and the Sea of Okhotsk. The East Asian activity center of the wave train, corresponding to descending motion, moves westward from Japan to the Northeast China-Siberia region with the evolution of the NABS+. During the NABS+ development stage (Figs. 11a–c), high-pressure anomalies over Japan and low-pressure anomalies over Northeast China jointly lead to low-level southerly wind anomalies prevailing from South China to Northeast China. This promotes warm and moist water vapor transport from the Indian Ocean and the South China Sea to North China and converges locally (Figs. 11g–i). During the NABS+ decaying stage, the anomalous high pressure and related anticyclone intensify and move westward to Northeast China, inducing northerly wind anomalies prevailing from South China to Northeast China (Figs. 11d–f), and thereby inhibiting water vapor transport to North China (Figs. 11j–l). Water vapor exhibits a narrow and enhanced divergence band along the Shandong Peninsula to the upper reaches of the Yellow River, whose position is consistent with the drought center in North China. It is noteworthy that the signs of precipitation and water vapor divergence are not coherent in some regions such as the Huang-Huai River Basin, but match well in their centers such as the Shandong Peninsula, the upper reaches of the Yellow River and Southwest China. During the mature stage of NABS, the anomalous high pressure previously located in Japan moves to Northeast China, with its intensity being weaker than that in the NABS+ decaying stage (Figs. 11c–d).

Figure 12 displays the possible processes and mechanisms by which the NABS forces precipitation interdecadal variations over China in the ATL experiment. North Atlantic SST anomalies can trigger a mid-latitude wave train across Eurasia, and its East Asian atmospheric activity centers tend to move westward with NABS+ evolution. During the mature stages of the NABS+, descending motion over Northeast China leads to low-level southerly wind anomalies, which promote water vapor convergence over North China and a local precipitation increase. Insufficient precipitation mainly occurs over Southwest China. During the development and decaying stages of the NABS+, as the atmospheric activity center over East Asia intensifies and moves westward from Japan to Northeast China, the precipitation pattern varies. In terms of the low-level wind field from South China to Northeast China, the NABS+ development stage is accompanied with southerly wind anomalies, whereas the NABS+ decaying stage is accompanied with northerly wind anomalies.

6. The combined North Pacific-North Atlantic interdecadal SST experiment (CPA experiment)

The PAC and ATL experiments are forced by the PDO-related North Pacific SST anomalies and the NABS-related North Atlantic SST anomalies, respectively. These experiments reveal the precipitation response to SST effects from a single North Pacific or North Atlantic source. The MPA experiment further simulates the precipitation response to the interdecadal SST forcing in both the North Pacific and North Atlantic, aiming to answer the following questions:

1) What are the response characteristics of precipitation over China jointly forced by the PDO and NABS modes?

2) What are the interdecadal synergistic effects of the North Pacific and North Atlantic SST anomalies on precipitation over China?

In addressing these questions, we perform a coupled reconstruction for the combined climate field at a 24-year cycle, including SST forcing, simulated precipitation, sea level pressure, 500-hPa geopotential height, 850-hPa wind, and vertically integrated water vapor flux and its divergence. Phase 0° is artificially defined as the onset of warm SST anomalies in the CNP, consistent with the analyses in the PAC experiment. It should be pointed out that the reconstructed spatiotemporal evolution of the North Pacific and North Atlantic SST obtained from the CPA experiment (figure not shown) are highly similar to those in Figure 1b, just with a larger amplitude. During the first 1/4 cycle of the PDO− development stage, the NABS+ weakens, while during the post 1/4 cycle of the PDO− decaying stage, the NABS− develops.

6.1 Interdecadal pattern of precipitation

Figure 13 illustrates the half-cycle evolution of the simulated precipitation over China driven by the North Pacific and North Atlantic SST forcing. The simulated precipitation anomalies over China display a meridional dipole pattern bounded by 32°N, with negative (positive) anomalies south (north) of the MLYR (Figs. 13a–d). This meridional dipole pattern of precipitation anomalies intensifies during the first 1/4 cycle and weakens during the subsequent 1/4 cycle. To further elucidate the patterns of the SST forcing and simulated precipitation responses associated with the PDO and NABS in the CPA experiment, we perform composite analyses (Fig. 14). The results indicate that during the PDO+, the simulated precipitation anomalies over China show a "south flooding and north drought" pattern with positive (negative) anomalies over the south (north) of the MLYR (Fig. 14c). During the NBAS+, the simulated precipitation anomalies exhibit a "south drought and north flooding" pattern with a precipitation increase from the Yangtze River to the Yellow River and a precipitation decrease over South China (Fig. 14 d). Similar precipitation distribution characteristics over China are evident in the observation during the PDO+ and NBAS+ (Figs. 14e,f). Notably, a distinct interdecadal northward shift of rainbands and drought bands can be observed (Fig. 13g), aligning with both timing and location as observed (Fig. 13h). These results indicate that under the joint forcing of the North Pacific and North Atlantic SST, the model can capture, to some extent, observed precipitation features, including interdecadal distribution patterns and the northward shift of rainbands.

6.2 Synergistic effects of the SST on the interdecadal northward shift of rainbands

How do the North Pacific and North Atlantic SST jointly influence the interdecadal northward shifts of rainbands? The temporal sequence of SST anomalies associated with the PDO and NABS may wield crucial influence. On a 24-year time scale, the PDO and NABS mature stages are asynchronous (Figs. 3c,8c), and their emergence sequences are the PDO+, NABS+, PDO− and NABS−. During the mature stage of the PDO+, the simulated precipitation increases over the south of the MLYR. During the NABS+ mature stage, the simulated precipitation increases over the Yangtze-Huang River region. Consequently, the rainband migrates northward from the south of MLYR to the Yangtze-Huang River region as the PDO+ transitions to the NABS+. It is precisely due to the synergistic effects of the PDO and NABS that different atmospheric circulation fields are induced, directly resulting in the interdecadal northward shifts of rainbands as observed. Unlike the PAC and ATL experiments, which solely involve SST effects from a single ocean basin, the CPA experiment includes SST effects from both ocean basins. Therefore, the North Atlantic (North Pacific) SST influences precipitation interdecadal variations when the PDO (NABS) is dominant, and the responses of precipitation and related atmospheric circulations to SST can be obtained by subtracting the results of the PAC or ATL experiment from those of the CPA experiment.

During the PDO+ mature stage, the NABS mode transitions from a cold phase to a warm phase. In the North Atlantic, cold SST anomalies prevails over the entire basin, with maximum values occurring in the subpolar regions (Fig. 14a). These large-scale cold SST anomalies in the North Atlantic can affect atmospheric circulation over East Asia through a mid-latitude wave train across Eurasia triggered by the NAO+ (Fig.

15a). Subsequently, anomalous low pressure occupies the western Pacific south of 30°N and the land of East Asia, while high-pressure anomalies only control the east of the Korean Peninsula-Honshu Island region. As a result, an anomalous anticyclonic circulation exists east of the Korean Peninsula-Honshu, bringing easterly wind anomalies along 30°N to its south side (Fig. 16d). Over the South China Sea, an anomalous cyclonic circulation can be found, bringing the southwesterly wind anomalies from the Indian Ocean to South China. Water vapor budget analyses reveal that warm and humid water vapor originating from the Indian Ocean only reaches South China and converges locally (Fig. 16g). However, the signs of water vapor divergence and precipitation anomalies near the Shandong Peninsula do not match, suggesting potential dominance of other processes in causing the drought over this region.

As the PDO+ transitions to the NABS+, large-scale warm SST anomalies are found in the North Pacific (Fig. 14b), which trigger a mid-latitude wave train (Fig. 15b), thus resulting in an anomalous cyclonic circulation over the Northeast China-Japan region and an anomalous anticyclonic circulation south of the MLYR (Fig. 16e). The circulation configuration over East Asia leads to southerly wind anomalies prevailing from the South China Sea to the Shandong Peninsula, facilitating the northward water vapor transport to North China and water vapor convergence there (Fig. 16h). Hence, precipitation over the north of the MLYR increases (Fig. 16b).

7. Conclusions and discussions

Deciphering the intricate interplay between multi-timescale SST forcing and precipitation response over China poses a challenge due to signal superposition. Limited studies have explored the relationship of the precipitation with SST at a specific frequency band. In this research, employing the MTM–SVD method for signal separation and spatiotemporal reconstruction, we utilize the ECHAM5 simulations to investigate the individual and synergistic effects of the North Pacific and North Atlantic SST forcing on precipitation over China. Our investigation also unveils the possible processes and potential influence mechanisms involved on interdecadal time scales. The results indicate that the ECHAM5 successfully replicates the periodic precipitation responses over China under the SST interdecadal forcing (with a 24-year cycle) in distinct regions (single North Pacific, single North Atlantic and both regions). Different precipitation patterns emerge in response to the individual effects of the PDO and NABS, and their combined effects can contribute to an observed interdecadal northward shift of rainband over China.

Under the interdecadal forcing of the North Pacific SST, the PDO correlates closely with a tri-polar pattern of precipitation anomalies over China. During the PDO− phase, precipitation increases over the MLYR and decreases over North China and South China. There are two mechanisms that govern the modification of the precipitation over China by North Pacific SST anomalies associated with the PDO−. First, cold SST anomalies along the North American west coast weaken the AL, triggering an NAO atmospheric response in the North Atlantic. This induces high-pressure anomalies over northern East Asia through a mid-latitude wave train across Eurasia. Second, the mid-latitude wave train and the convective enhancement due to SST anomalies over the central-western North Pacific jointly weaken the WPSH. The combined effects of the anomalous high pressure over northern East Asia and the weak WPSH lead to northerly and southerly wind anomalies over the south and north of the MLYR, thereby resulting in a precipitation decrease over the MLYR and a precipitation increase over South China and North China.

In terms of the interdecadal forcing of the North Atlantic SST, the NABS exhibits a positive correlation with precipitation over North China and a negative correlation with precipitation over Southwest China. The NABS can induce a mid-latitude wave train propagating eastward from the North Atlantic to East Asia, and atmospheric activity centers over East Asia undergo a westward shift trend with NABS+ evolution. During the development and mature stages of the NABS+, the anomalous high pressure over northern East Asia and the anomalous low pressure west of it induce southerly wind anomalies from South China to Northeast China, contributing to water vapor convergence over North China and a local precipitation increase. As the NABS+ decays, northerly wind anomalies prevail from South China to Northeast China, causing a narrow and intensified water vapor divergence zone over northern China, and resulting in insufficient precipitation locally.

Under the combined interdecadal forcing of the SST in the North Pacific and North Atlantic, precipitation anomalies over China show a meridional dipole distribution bounded by 32°N, and rainbands display an observed northward motion.

During the PDO+ (NABS+) phase, the rainbands are located over South (North) China. The transition from PDO+ to NABS+ underscores the synergistic effects of the North Pacific and North Atlantic SST on the interdecadal northward shift of rainbands. The combined SST effects in the North Pacific and North Atlantic, to some extent, explains the observed interdecadal variation in precipitation over China.

This study acknowledges certain limitations that warrant further consideration. Firstly, the interdecadal SST variations in the North Pacific and North Atlantic may exert a dominant controlling effect on precipitation in distinct regions. Specifically, the most pronounced interdecadal signal of precipitation response appears over the MLYR under the PDO forcing, while it appears over North China under the NABS forcing. For the precipitation response in different regions, there is a frequency shift phenomenon, and the obvious dominant cycles shift from a 24-year period in the SST forcing fields to a 32-year period in the simulations. These frequency shifts may be related to the internal dynamic processes of the atmosphere. A comprehensive analysis is requisite to delve deeper into the dominant controlling effects and frequency shifts of the simulated precipitation. Secondly, existing studies have highlighted the interdecadal variabilities of the Indian Ocean SST (Cole et al., 2000; Tozuka et al., 2007; Abram et al., 2008; Du et al., 2013). For instance, the impact of the Indian Ocean Basin mode on the summer climate over East Asia also exhibits marked interdecadal shifts (Huang et al., 2010). It is imperative to note that the current study exclusively focuses on the influences of the SST in the North Pacific and North Atlantic. Future explorations should encompass an investigation into the potential effects of the SST in the Indian Ocean. Additionally, since both precipitation and SST exhibit variabilities across multiple time scales (e.g., Ding et al., 2020a; Wu et al., 2023), forthcoming research endeavors should extend to examine the modulation of SST variabilities on precipitation variations in China at different time scales, such as the modulation of high-frequency variations (i.e., interannual or seasonal variability) by interdecadal variability.

Acknowledgments This work is supported by the National Natural Science Foundation of China (NSFC; Grant No. 42030410), Laoshan Laboratory (No. LSKJ202202403 and LSKJ202202402), the Strategic Priority Research Program of the Chinese Academy of Sciences (CAS; Grant No. XDB40000000), the Startup Foundation for Introducing Talent of NUIST.

Competing interests

The authors declare no competing interests.

Data availability statement

We thank the University of East Anglia Climatic Research Unit supplied the precipitation data (Harris et al., 2020) (https://crudata.uea.ac.uk/cru/data/hrg/), the Met Office Hadley Centre provided HadISST v1.1 data (Rayner et al., 2003) (https://hadleyserver.metoffice.gov.uk/hadisst/), and the Program for Climate Model Diagnosis and Intercomparison (PCMDI) provided the Atmospheric Model Intercomparison Project II Sea Surface Temperature and Sea Ice Concentration Boundary Conditions (https://pcmdi.llnl.gov/mips/amip/amip2/). We also thank the Max Planck Institute for Meteorology (MPI-M) for developing the Atmospheric General Circulation Model of the ECHAM5 (Roeckner et al., 2003) (https://mpimet.mpg.de/).

References

Abram N J, Gagan M K, Cole J E, Hantoro W S, and Mudelsee M (2008) Recent intensification of tropical climate variability in the Indian Ocean. Nature Geoscience 1: 849-853. 10.1038/ngeo357

Chang C P, Zhang Y S, and Li T (2000) Interannual and interdecadal variations of the East Asian summer monsoon and tropical Pacific SSTs. Part I: Roles of the subtropical ridge. Journal of Climate 13: 4310-4325. https://doi.org/10.1175/1520-0442(2000)013<4310:IAIVOT>2.0.CO;2

Chen L, Li G, Lu B et al. (2022) Two approaches of the spring North Atlantic sea surface temperature affecting the following July precipitation over central China: The tropical and extratropical pathways. Journal of Climate 35: 2969-2986. https://doi.org/10.1175/JCLI-D-21-1012.1

Chen W, Feng J, and Wu R G (2013) Roles of ENSO and PDO in the Link of the East Asian Winter Monsoon to the following Summer Monsoon. Journal of Climate 26: 622-635. https://doi.org/10.1175/JCLI-D-12-00021.1

Cole J E, Dunbar R B, McClanahan T R, and Muthiga N A (2000) Tropical Pacific forcing of decadal SST variability in the western Indian Ocean over the past two centuries. Science 287: 617-619. https://doi.org/10.1126/science.287.5453.617

Ding Y H, Wang Z Y, and Sun Y (2008) Inter‐decadal variation of the summer precipitation in East China and its association with decreasing Asian summer monsoon. Part I: Observed evidences. International Journal of Climatology 28: 1139-1161. https://doi.org/10.1002/joc.1615

Ding Y H, Liang P, Liu Y J, and Zhang Y C (2020a) Multiscale Variability of Meiyu and Its Prediction: A New Review. Journal of Geophysical Research: Atmospheres 125: e2019JD031496. https://doi.org/10.1029/2019JD031496

Ding Y H, Li Y, Wang Z Y, Si D, and Liu Y J (2020b) Interdecadal variation of Afro-Asian summer monsoon: coordinated effects of AMO and PDO oceanic modes (in Chinese). Transactions of Atmospheric Sciences 43: 20-32.

Dong X (2016) Influences of the Pacific Decadal Oscillation on the East Asian Summer Monsoon in non-ENSO years. Atmospheric Science Letters 17: 115-120. https://doi.org/10.1002/asl.634

Dong X, Xue F, and Zeng Q C (2014) Observational analysis and numerical simulation of the Decadal Variation in the relationship between the Aleutian Low and the Iceland Low during Boreal Winter (in Chinese). Climatic and Environmental Research 19: 523-535.

https://doi.org/10.3878/j.issn.1006-9585.2013.13021

Du J Y, Tao L, and Xu C Y (2022) Interdecadal variation of land precipitation in China and relative contributions of global warming，IPO and AMO (in Chinese). Acta Meteorologica Sinica 80: 685-700. 10.11676/qxxb2022.055

Du Y, Cai W J, and Wu Y L (2013) A New Type of the Indian Ocean Dipole since the Mid-1970s. Journal of Climate 26: 959-972. https://doi.org/10.1175/JCLI-D-12-00047.1

Harris L, Osborn T J, Jones P, and Lister D (2020) Version 4 of the CRU TS monthly high-resolution gridded multivariate climate dataset. Scientific data 7: 109. https://doi.org/10.1038/s41597-020-0453-3

Honda M, Nakamura H, Ukita J, Kousaka I, and Takeuchi K (2001) Interannual Seesaw between the Aleutian and Icelandic Lows. Part I: Seasonal Dependence and Life Cycle. Journal of Climate 14: 1029-1042. https://doi.org/10.1175/1520-0442(2001)014<1029:ISBTAA>2.0.CO;2

Hu J Y, Wang H N, Gao C, Zhou L, and Zhang R-H (2023) Interdecadal wind stress variability over the tropical Pacific causes ENSO diversity in an intermediate coupled model. Climate Dynamics 60: 1831-1847. https://doi.org/10.1007/s00382-022-06414-x

Hu K M, Liu Y X, Huang G, He Z Q, and Long S-M (2020) Contributions to the interannual summer rainfall variability in the mountainous area of central China and their decadal changes. Advances in Atmospheric Sciences 37: 259-268. https://doi.org/10.1007/s00376-019-9099-5

Huang G, Hu K M, and Xie S-P (2010) Strengthening of Tropical Indian Ocean Teleconnection to the Northwest Pacific since the Mid-1970s: An Atmospheric GCM Study. Journal of Climate 23: 5294-5304. https://doi.org/10.1175/2010JCLI3577.1

Lau K-M, and Li M-T (1984) The Monsoon of East Asia and its Global Associations—A Survey. Bulletin of the American Meteorological Society 65: 114-125. https://doi.org/10.1175/1520-0477(1984)065<0114:TMOEAA>2.0.CO;2

Li J P, Zheng F, Sun C, Feng J, and Wang J (2019) Pathways of Influence of the Northern Hemisphere Mid-high Latitudes on East Asian Climate: A Review. Advances in Atmospheric Sciences 36: 902-921. 10.1007/s00376-019-8236-5

Li J P, Ren R C, Qi Y Q et al. (2013) Progress in Air-Land-Sea Interactions in Asia and Their Role in Global and Asian Climate Change (in Chinese). Chinese Journal of Atmospheric Sciences 27: 21.

Li W J, Liu J P, Ren H L, and Zuo J Q (2018) Characteristics and Corresponding Mechanisms of the Leading Modes of Interdecadal Variability of Summer Rainfall in Southern China (in Chinese). Journal of Atmospheric Sciences 4: 859-876. doi:10.3878/j.issn.1006-9895.1802.17283

Li X, Zhou W, Chen D, Li C, and Song J (2014) Water vapor transport and moisture budget over eastern China: Remote forcing from the two types of El Niño. Journal of Climate 27: 8778-8792. https://doi.org/10.1175/JCLI-D-14-00049.1

Liang P, Chen L J, Ding Y H, He J, and Zhou B (2018) Relationship between long-term variability of Meiyu over the Yangtze River and ocean and Meiyu's predictability study (in Chinese). Acta Meteorologica Sinica 76: 379-393.

Liu J, Wang H, Lu E, and Kumar A (2019) Decadal modulation of East China winter precipitation by ENSO. Climate Dynamics 52: 7209-7223. https://doi.org/10.1007/s00382-016-3427-6

Liu Y Y, Hu Z-Z, and Wu R G (2020) Cooperative effects of tropical Pacific and Atlantic SST forcing in southern China winter precipitation variability. Climate Dynamics 55: 2903-2919. https://doi.org/10.1007/s00382-020-05430-z

Lyu J M, Zhu C W, and Ju J H (2014) Interdecadal variability in summer precipitation over East China during the past 100 years and its possible causes (in Chinese). Chinese Journal of Atmospheric Sciences 38: 782-794.

Mann M E, and Park J (1994) Global-scale modes of surface temperature variability on interannual to century timescales. Journal of Geophysical Research 99: 25819. 10.1029/94JD02396

Mann M E, and Park J (1999) Oscillatory Spatiotemporal Signal Detection in Climate Studies: A Multiple-Taper Spectral Domain Approach. Advances in Geophysics 41: 1-131.

Mantua N J, Hare S R, Zhang Y, Wallace J M, and Francis R C (1997) A Pacific interdecadal climate oscillation with impacts on salmon production. Bulletin of the American Meteorological Society 78: 1069-1080. https://doi.org/10.1175/1520-0477(1997)078%3C1069:APICOW%3E2.0.CO;2

Qian C, and Zhou T J (2014) Multidecadal Variability of North China Aridity and Its Relationship to PDO during 1900–2010. Journal of Climate 27: 1210-1222. https://doi.org/10.1175/JCLI-D-13-00235.1

Qiao S B, Chen D, Wang B et al. (2021) The longest 2020 Meiyu season over the past 60 years: Subseasonal perspective and its predictions. Geophysical Research Letters 48: e2021GL093596. https://doi.org/10.1029/2021GL093596

Rayner N, Parker D E, Horton E et al. (2003) Global analyses of sea surface temperature, sea ice, and night marine air temperature since the late nineteenth century. Journal of Geophysical Research: Atmospheres 108: 4407. https://doi.org/10.1029/2002JD002670

Roeckner E, Bäuml G, Bonaventura L et al. (2003) The atmospheric general circulation model ECHAM 5. PART I: Model description.

Si D, and Ding Y H (2016) Oceanic Forcings of the Interdecadal Variability in East Asian Summer Rainfall. Journal of Climate 29: 7633-7649. https://doi.org/10.1175/JCLI-D-15-0792.1

Thomson D J (1982) Spectrum estimation and harmonic analysis. Proceedings of the IEEE 70: 1055-1096.

Tourre Y M, Rajagopalan B, and Kushnir Y (1999) Dominant Patterns of Climate Variability in the Atlantic Ocean during the Last 136 Years. Journal of Climate 12: 2285-2299. http://dx.doi.org/10.1175/1520-0442(1999)0122.0.CO;2

Tozuka T, Luo J-J, Masson S, and Yamagata T (2007) Decadal Modulations of the Indian Ocean Dipole in the SINTEX-F1 Coupled GCM. Journal of Climate 20: 2881-2894. https://doi.org/10.1175/JCLI4168.1

Wang J X, Zhu X F, Liu X F, and Pan Y Z (2018) Research on agriculture drought monitoring method of Henan Province with multi-sources data (in Chinese). Remote Sensing for Natural Resources 30: 180-186.

Wang Y M, Li S L, and Luo D H (2009) Seasonal response of Asian monsoonal climate to the Atlantic Multidecadal Oscillation. Journal of Geophysical Research: Atmospheres 114: D02112. https://doi.org/10.1029/2008JD010929

Wei F Y, Zhang T, and Han X (2013) MTM-SVD approach and its application in the spatio-temporal variability analysis of SST of the Indian Ocean and precipitation of South China (in Chinese). Marine Science Bulletin 32: 133-140. 10.11840/j.issn.1001-6392.2013.02.003

Wu M M, and Wang L (2019) Enhanced correlation between ENSO and western North Pacific monsoon during boreal summer around the 1990s. Atmospheric and Oceanic Science Letters 15: 376-384. https://doi.org/10.1080/16742834.2019.1641397

Wu M M, Zhang R-H, Hu J Y, and Zhi H (2023) Synergistic Interdecadal Evolution of Precipitation over Eastern China and the Pacific Decadal Oscillation during 1951–2015. Advances in Atmospheric Sciences 41: 53–72. https://doi.org/10.1007/s00376-023-3011-z

Wu Z W, Wang B, Li J P, and Jin F-F (2009) An empirical seasonal prediction model of the east Asian summer monsoon using ENSO and NAO. Journal of Geophysical Research: Atmospheres 114: D18120. https://doi.org/10.1029/2009JD011733

Wu Z W, Li J P, Jiang Z H, He J H, and Zhu X Y (2012) Possible effects of the North Atlantic Oscillation on the strengthening relationship between the East Asian Summer monsoon and ENSO. International Journal of Climatology 32: 794-800. https://doi.org/10.1002/joc.2309

Zhang J-Y, Wang L, Yang S, Chen W, and Huangfu J L (2016a) Decadal changes of the wintertime tropical tropospheric temperature and their influences on the extratropical climate. Science Bulletin 61: 737-744. https://doi.org/10.1007/s11434-016-1054-6

Zhang M Q, Sun J Q, and Gao Y Q (2022a) Impacts of North Atlantic sea surface temperature on the predominant modes of spring precipitation monthly evolution over Northeast China. Climate Dynamics 58: 1383-1401. https://doi.org/10.1007/s00382-021-05966-8

Zhang R-H, and Levitus S (1997) Structure and cycle of decadal variability of upper-ocean temperature in the North Pacific. Journal of Climate 10: 710-727. https://doi.org/10.1175/1520-0442(1997)010<0710:SACODV>2.0.CO;2

Zhang R-H, and Gao C (2016) The IOCAS intermediate coupled model (IOCAS ICM) and its real-time predictions of the 2015–2016 El Niño event. Science Bulletin 61: 1061-1070. https://doi.org/10.1007/s11434-016-1064-4

Zhang R-H, Gao C, and Feng L C (2022b) Recent ENSO evolution and its real-time prediction challenges. National Science Review 9: nwac052. https://doi.org/10.1093/nsr/nwac052

Zhang R-H, Yu Y Q, Song Z Y et al. (2020) A review of progress in coupled ocean-atmosphere model developments for ENSO studies in China. Journal of Oceanology and Limnology 38: 930-961. https://doi.org/10.1007/s00343-020-0157-8

Zhang R, Min Q, and Su J (2017) Impact of El Niño on atmospheric circulations over East Asia and rainfall in China: Role of the anomalous western North Pacific anticyclone. Science China Earth Sciences 60: 1124-1132. https://doi.org/10.1007/s11430-016-9026-x

Zhang W J, Jin F-F, Stuecker M F et al. (2016b) Unraveling El Niño's impact on the East Asian Monsoon and Yangtze River summer flooding. Geophysical Research Letters 43: 375-311,382. https://doi.org/10.1002/2016GL071190

Zhang Z Q, Sun X G, and Yang X-Q (2018) Understanding the Interdecadal Variability of East Asian Summer Monsoon Precipitation: Joint Influence of

Three Oceanic Signals. Journal of Climate 31: 5485-5506. https://doi.org/10.1175/JCLI-D-17-0657.1

Zhi H, Yu Y-Q, Yan L, Zhang W J, and Li Z Q (2012) Retrospective prediction in a coupled model over East Asia during El Nio decaying phase (in Chinese). Acta Meteorologica Sinica 70: 779-788.

Zhou T J, Wu B, and Dong L (2014) Advances in research of ENSO changes and the associated impacts on Asian-Pacific climate. Asia-Pacific Journal of Atmospheric Sciences 50: 405-422. https://doi.org/10.1007/s13143-014-0043-4

Zhou Z-Q, Xie S-P, and Zhang R (2021) Historic Yangtze flooding of 2020 tied to extreme Indian Ocean conditions. Proceedings of the National Academy of Sciences 118: e2022255118. https://doi.org/10.1073/pnas.2022255118

Zhu Y L, Wang H J, Ma J H, Wang T, and Sun J Q (2015) Contribution of the phase transition of Pacific Decadal Oscillation to the late 1990s' shift in East China summer rainfall. Journal of Geophysical Research: Atmospheres 120: 8817-8827. https://doi.org/10.1002/2015JD023545

Table 1 The design of model sensitivity experiments.

Names of the Interdecadal SST Experiments	Forcing field of the SST	Integration time
Control（CTL experiment）	climatological	1951–2020
Pacific（PAC experiment）	climatological + North Pacific	
Atlantic（ATL experiment）	climatological + North Atlantic	
Combined Pacific-Atlantic（CPA experiment）	climatological+ North Pacific+North Atlantic	

Table 2 The selected periods of the PDO+ and PDO− (with a 1-time standard deviation as the threshold) for the composite analyses.

	Periods
PDO+	1978.04–1987.10 (115 months)
PDO−	1965.01–1973.09, and 2003.03–2009.10 (185 months)

Table 3 The selected periods of the NABS+ and NABS− (with a 1-time standard deviation as the threshold) for the composite analyses.

	Periods
NABS+	1961.07–1968.04; 1999.01–2005.09 (163 months)
NABS−	1973.06–1983.06 (121 months)

Figure Captions

Figure 1. (a) The LFV spectrum of precipitation (mm mon^{-1}) over China during 1951–2020, with a red asterisk corresponding to a significant interdecadal peak. (b) The half-cycle spatiotemporal evolution of SST (°C). (c) The interdecadal SST signals of the mid-latitude North Pacific (170°W, 40°N; violet asterisk in b) and mid-latitude North Atlantic (40°W, 40°N; green asterisk in b). (b, c) are derived from the joint reconstruction of precipitation and SST at the 24.4-year cycle. The blue boxes in (b) are the domain with which SST anomalies are used for the PAC, ATL, and CPA experiments.

Figure 2. Normalized time series of precipitation (a–c; mm mon^{-1}) and corresponding wavelet power spectrums (d–f; mm^2 mon^{-2}) simulated by the (a, d) PAC, (b, e) ATL and (c, f) CPA experiments: North China (NCHN; 105°–122°E, 34°–42°N; gray lines), the MLYR (105°–122°E, 28°–34°N; blue lines) and South China (SCHN; 105°–120°E, 21°–28°N; purple lines).

Figure 3. (a) The time-latitude section of the simulated precipitation (mm mon^{-1}) zonally-averaged (110°–122°E), (b) the time-longitude section of the North Pacific SST forcing (°C) meridionally-averaged (28°–45°N), and the (c) time series of the reconstructed PDO index. (a, b, and c) are obtained from the 24-year cycle reconstruction of the joint field associated with the PAC experiment. The red (blue) shadings in (c) are for the value greater (less) than 1-time the standard deviation and the gray line is the raw SST signal in the corresponding area. Composite analyses of

the (d) simulated precipitation and the (e) North Pacific SST with respect to the reconstructed PDO index. The dots represent at or above the 90% confidence level. The box in (e) represents the domain (170°E–150° W, 28°N–45°N) used to calculate the PDO index.

Figure 4. The half-cycle spatiotemporal evolution (Phases 0°–150°) of (a) the precipitation (mm mon^{-1}) over China, and of (b) the SST (shading; ℃) and SLP (contour; Pa) in the North Pacific. The results are obtained from the 24-year cycle reconstruction of the joint fields associated with the PAC experiment. The contour interval is 80 Pa for the SLP in (b).

Figure 5. The half-cycle spatiotemporal evolutions (a–f: Phases 0°–150°) of the 500-hPa GHT (gpm) from the North Atlantic to the North Pacific. The results are obtained from the 24-year cycle reconstruction of the joint fields associated with the PAC experiment.

Figure 6. The half-cycle spatiotemporal evolution (Phases 0°–150°): the (a–f) SLP (shading; Pa) and 850-hPa winds (vector; m s^{-1}), the (g–l) vertically integrated water vapor flux (vector; g m^{-1} s^{-1}) and its divergence (shading; g m^{-2} s^{-1}) over East Asia. The results are obtained from the 24-year cycle reconstruction of the joint fields associated with the PAC experiment.

Figure 7. Schematic diagram showing the processes and mechanisms by which the North Pacific interdecadal SST anomalies affect the precipitation over eastern China during the PDO−. At the surface (low panel), red (blue) shadings indicate warm (cold)

SST anomalies, and green (yellow) shadings indicate positive precipitation anomalies. At 500-hPa (top panel), red (blue) circles indicate anomalous anticyclonic (cyclonic) circulation. Black arrows indicate low-level winds, and red (blue) broad arrows indicate descending (ascending) motions of the atmosphere.

Figure 8 Same as in Figure 3 but for the ATL experiment during the NABS+. The box in (e) represents the domain (80°W–0°, 20°–65°N) used to calculate the NABS index. (b) The time-latitude section of the North Atlantic SST forcing (°C) zonally-averaged (80°W–0°).

Figure 9 Same as in Figure 4 but for the ATL experiment.

Figure 10. Same as in Figure 5 but from the North Atlantic to East Asia for the ATL experiment.

Figure 11 Same as in Figure 6 but for the ATL experiment.

Figure 12. Schematic diagram showing the processes and mechanisms by which the North Atlantic SST anomalies affect the precipitation over eastern China during mature stages of the NABS+. At the surface (low panel), red/blue (green/yellow) shadings indicate positive/negative SST (precipitation) anomalies. At 500-hPa (top panel), red (blue) circles indicate anomalous anticyclonic (cyclonic) circulation. Black arrows indicate low-level winds, and blue broad arrows indicate ascending motions of the atmosphere.

Figure 13. The half-cycle spatiotemporal evolution (a-f: Phases 0°–150°) of the (a)

precipitation (mm mon^{-1}) over China. Time-latitude sections of meridional (100°–120°E) mean precipitation of the (g) CPA experiment and (h) CRU observation reconstructed at the 24-year cycle.

Figure 14. Composite analyses of the (a, b) SST and (c–f) precipitation over eastern China associated with the observations and CPA experiment: (a, c, e) PDO+ minus PDO− and (b, d, f) NABS+ minus NABS−. Only values at or above the 90% confidence level are shown in (a, b); the dots denote the regression values exceeding the 90% confidence level in (c–f). The blue boxes in (c–f) indicate in-phase precipitation variations between observations and CPA experiment in the corresponding regions.

Figure 15. The SLP (shading; Pa) and 500-hPa GHT (contour; gpm) responses to the effects of SST: (a) NA_{PDO}, (b) NP_{NABS}, and (c) NP_{NABS} minus NA_{PDO}. The contours are the ±5, ±20, ±35, ±50 gpm. The NA_{PDO} (NP_{NABS}) is the composite analysis with respect to the PDO (NABS) phase based on the results of subtracting the PAC (ATL) experiment from the CPA experiment.

Figure 16. The atmospheric responses of the (a–c) precipitation (mm mon^{-1}), (d–f) 850-hPa winds (vector; m s^{-1}), and (g-i) vertically integrated water vapor flux (vector; g m^{-1} s^{-1}) and its divergence (shading; g m^{-2} s^{-1}) over East Asia to the North Atlantic SST forcing during the PDO+ (a, d, g; NA_{PDO}) and to the North Pacific SST forcing during $NABS^{+}$ (b, e, h; NP_{NABS}). (c, f, i) are the differences between NP_{NABS} and NA_{PDO} in precipitation, 850-hPa winds, and water vapor flux.

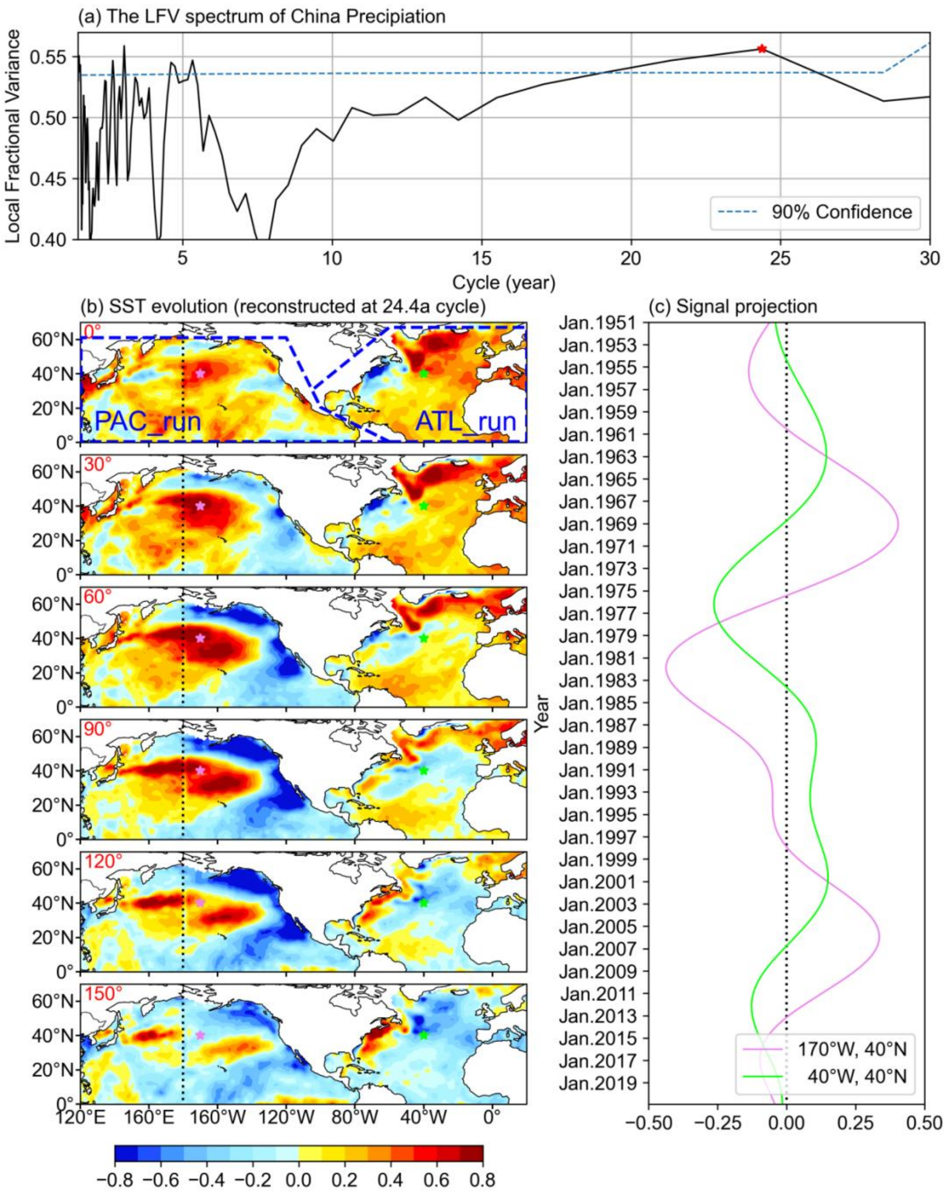

Figure 1. (a) The LFV spectrum of precipitation (mm mon^{-1}) over China during 1951–2020, with a red asterisk corresponding to a significant interdecadal peak. (b) The half-cycle spatiotemporal evolution of SST (°C). (c) The interdecadal SST signals of the mid-latitude North Pacific (170°W, 40°N; violet asterisk in b) and mid-latitude North Atlantic (40°W, 40°N; green asterisk in b). (b, c) are derived from the joint reconstruction of precipitation and SST at the 24.4-year cycle. The blue boxes in (b) are the domain with which SST anomalies are used for the PAC, ATL, and CPA experiments.

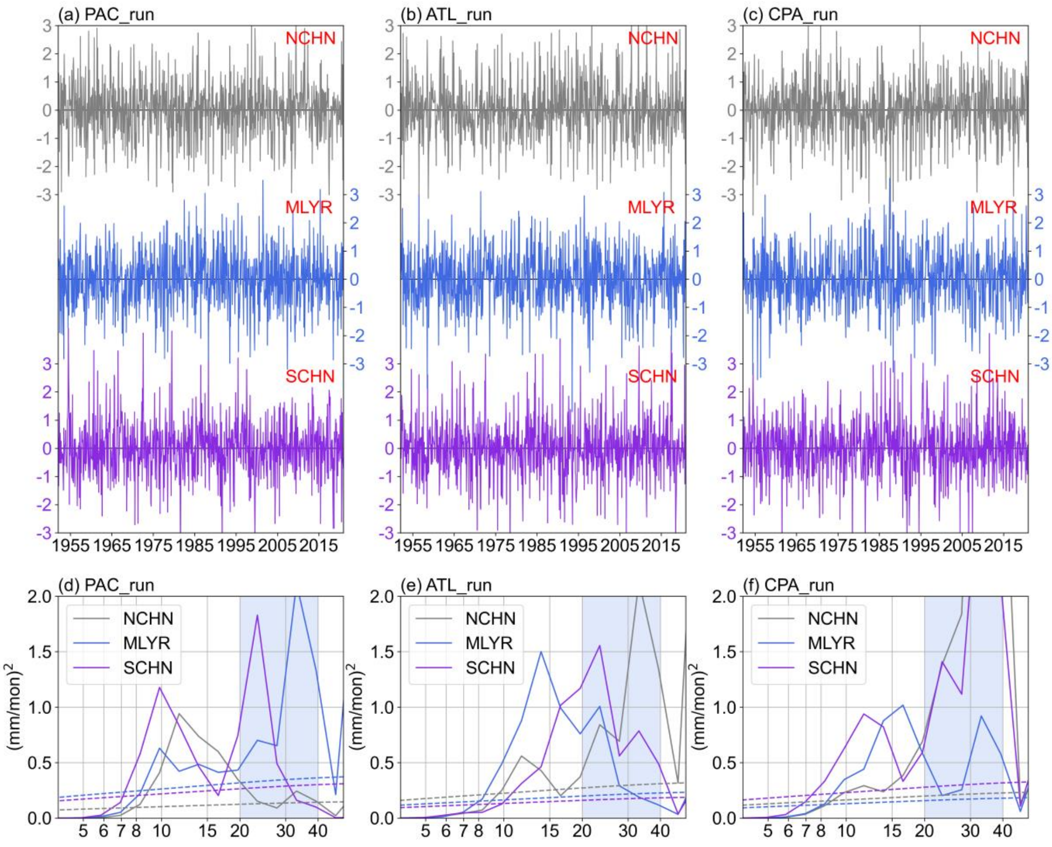

Figure 2. Normalized time series of precipitation (a–c; mm mon^{-1}) and corresponding wavelet power spectrums (d–f; mm^2 mon^{-2}) simulated by the (a, d) PAC, (b, e) ATL and (c, f) CPA experiments: North China (NCHN; 105°–122°E, 34°–42°N; gray lines), the MLYR (105°–122°E, 28°–34°N; blue lines) and South China (SCHN; 105°–120°E, 21°–28°N; purple lines).

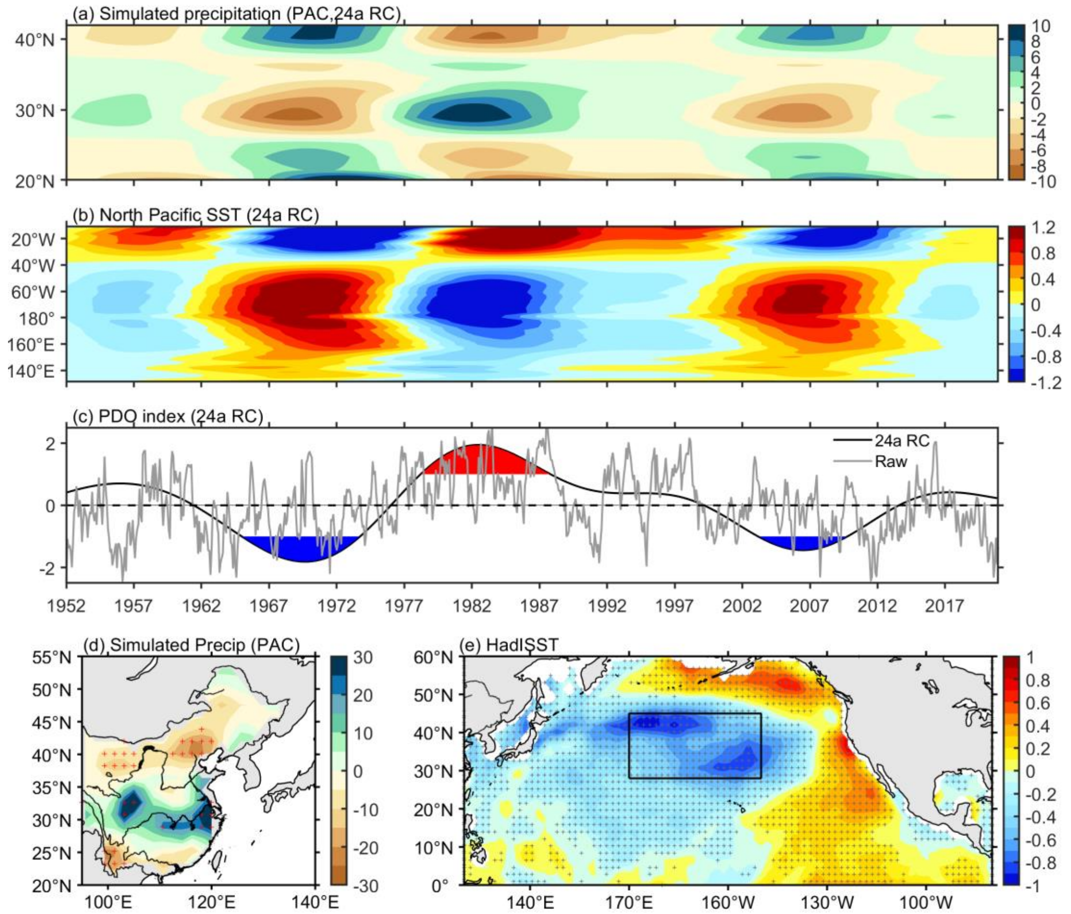

Figure 3. (a) The time-latitude section of the simulated precipitation (mm mon^{-1}) zonally-averaged (110°–122°E), (b) the time-longitude section of the North Pacific SST forcing (℃) meridionally-averaged (28°–45°N), and the (c) time series of the reconstructed PDO index. (a, b, and c) are obtained from the 24-year cycle reconstruction of the joint field associated with the PAC experiment. The red (blue) shadings in (c) are for the value greater (less) than 1-time the standard deviation and the gray line is the raw SST signal in the corresponding area. Composite analyses of the (d) simulated precipitation and the (e) North Pacific SST with respect to the reconstructed PDO index. The dots represent at or above the 90% confidence level. The box in (e) represents the domain (170°E–150° W, 28°N–45°N) used to calculate the PDO index.

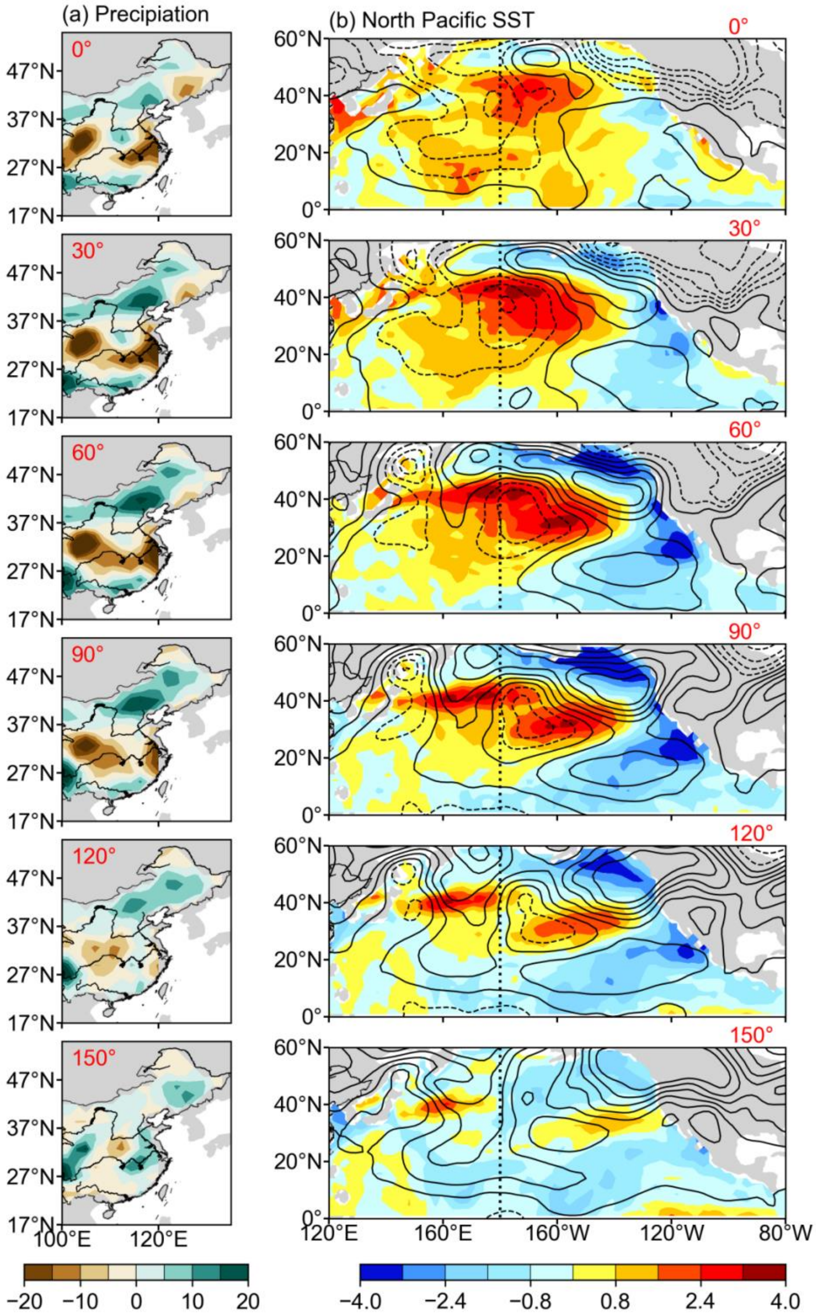

Figure 4. The half-cycle spatiotemporal evolution (Phases 0°–150°) of (a) the precipitation (mm mon^{-1}) over China, and of (b) the SST (shading; °C) and SLP (contour; Pa) in the North Pacific. The results are obtained from the 24-year cycle reconstruction of the joint fields associated with the PAC experiment. The contour interval is 80 Pa for the SLP in (b).

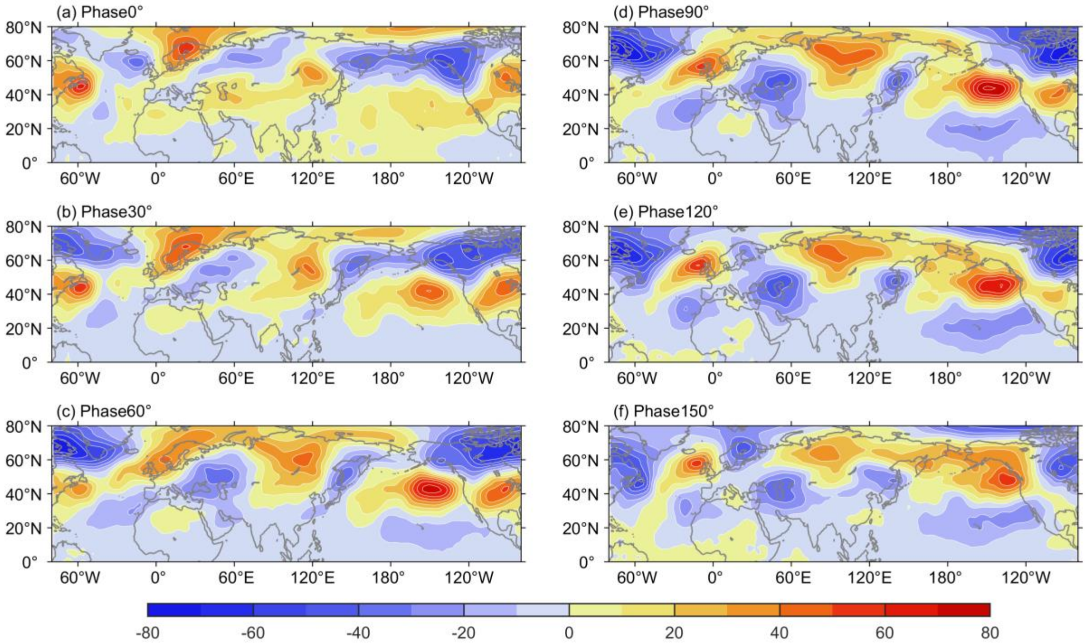

Figure 5. The half-cycle spatiotemporal evolutions (a–f: Phases 0°–150°) of the 500-hPa GHT (gpm) from the North Atlantic to the North Pacific. The results are obtained from the 24-year cycle reconstruction of the joint fields associated with the PAC experiment.

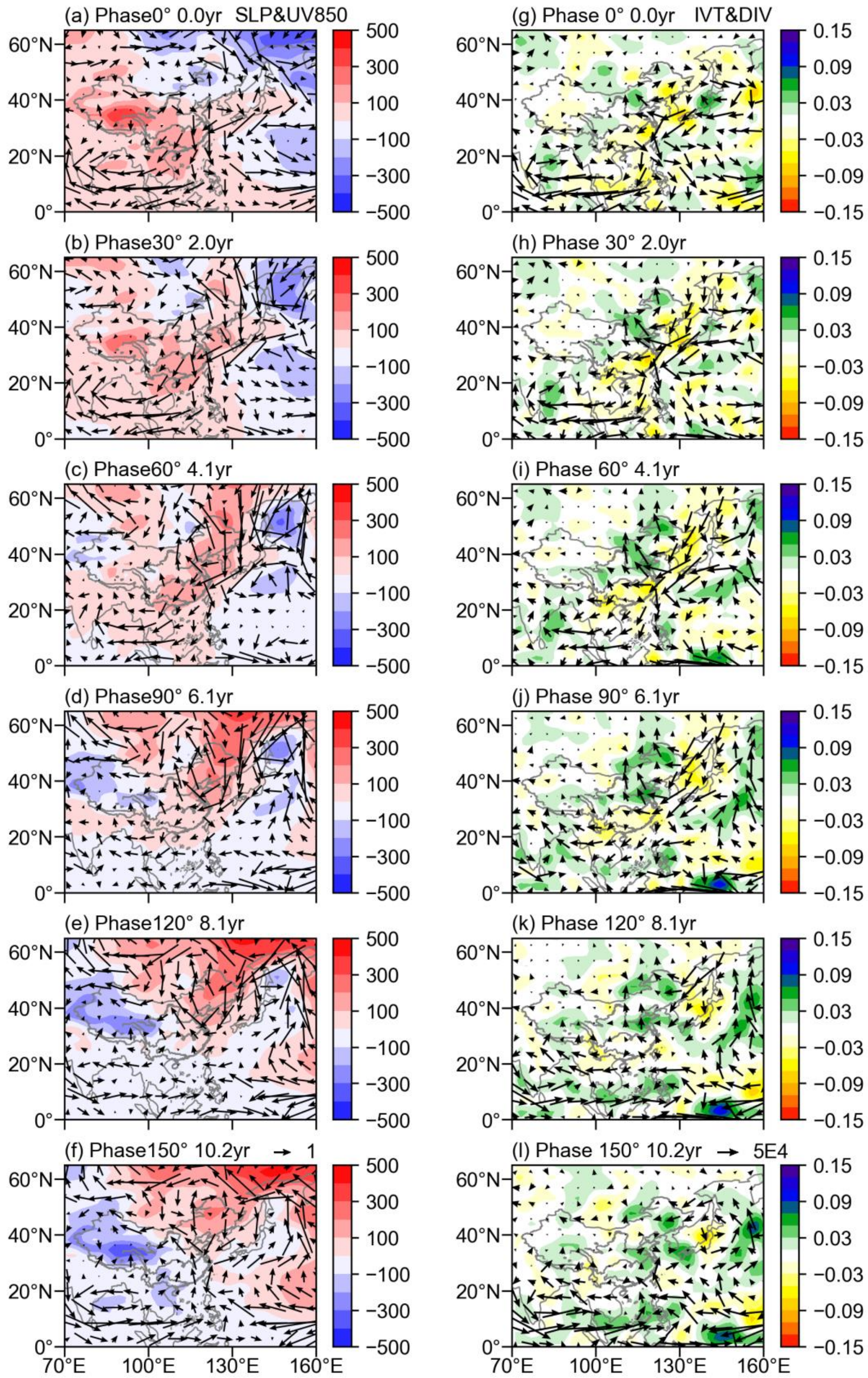

Figure 6. The half-cycle spatiotemporal evolution (Phases 0°–150°): the (a–f) SLP (shading; Pa) and 850-hPa winds (vector; m s^{-1}), the (g–l) vertically integrated water vapor flux (vector; g m^{-1} s^{-1}) and its divergence (shading; g m^{-2} s^{-1}) over East Asia. The results are obtained from the 24-year cycle reconstruction of the joint fields associated with the PAC experiment.

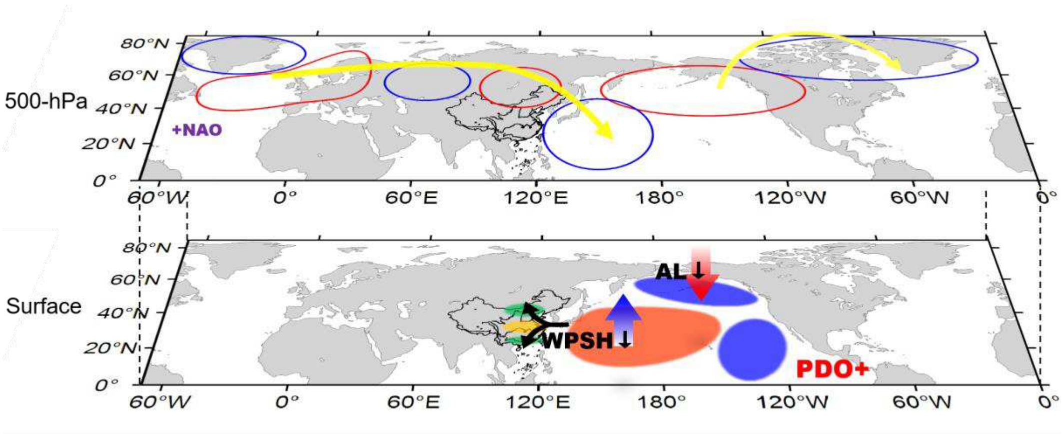

Figure 7. Schematic diagram showing the processes and mechanisms by which the North Pacific interdecadal SST anomalies affect the precipitation over eastern China during the PDO−. At the surface (low panel), red (blue) shadings indicate warm (cold) SST anomalies, and green (yellow) shadings indicate positive precipitation anomalies. At 500-hPa (top panel), red (blue) circles indicate anomalous anticyclonic (cyclonic) circulation. Black arrows indicate low-level winds, and red (blue) broad arrows indicate descending (ascending) motions of the atmosphere.

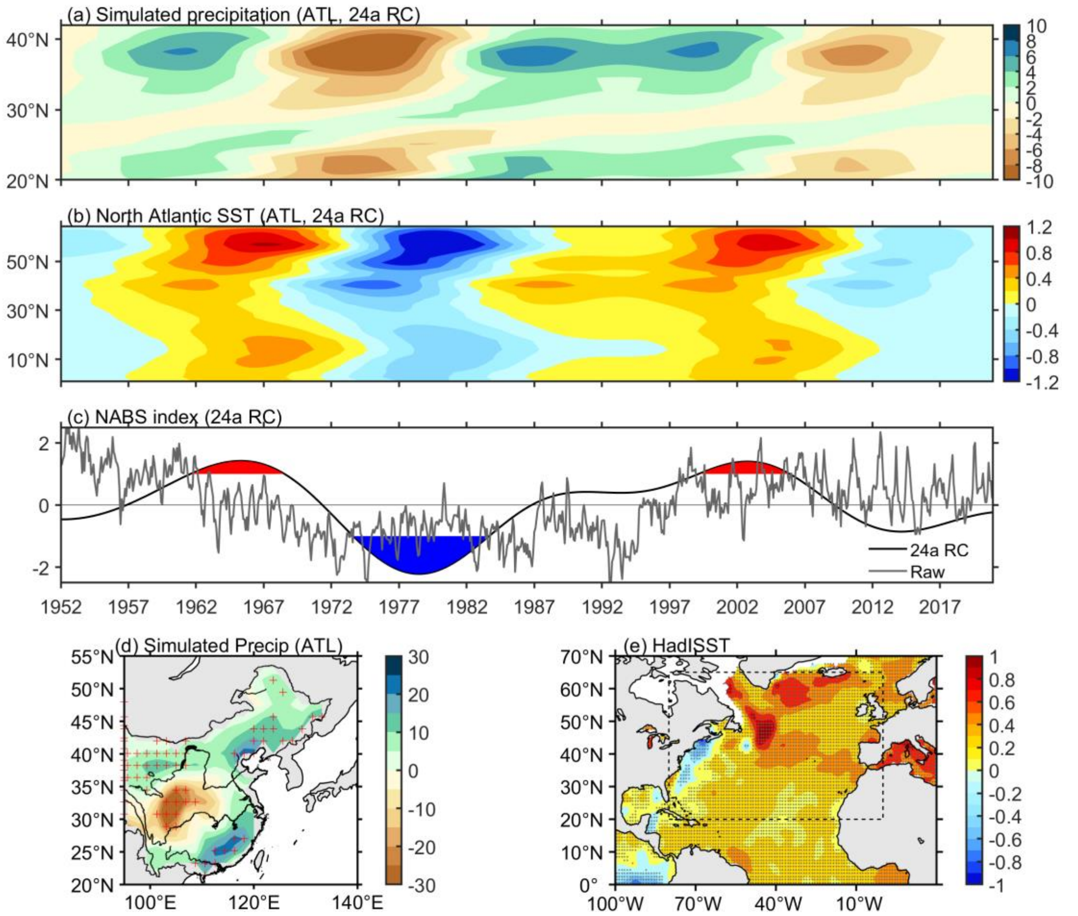

Figure 8 Same as in Figure 3 but for the ATL experiment during the NABS+. The box in (e) represents the domain (80°W–0°, 20°–65°N) used to calculate the NABS index. (b) The time-latitude section of the North Atlantic SST forcing (℃) zonally-averaged (80°W–0°).

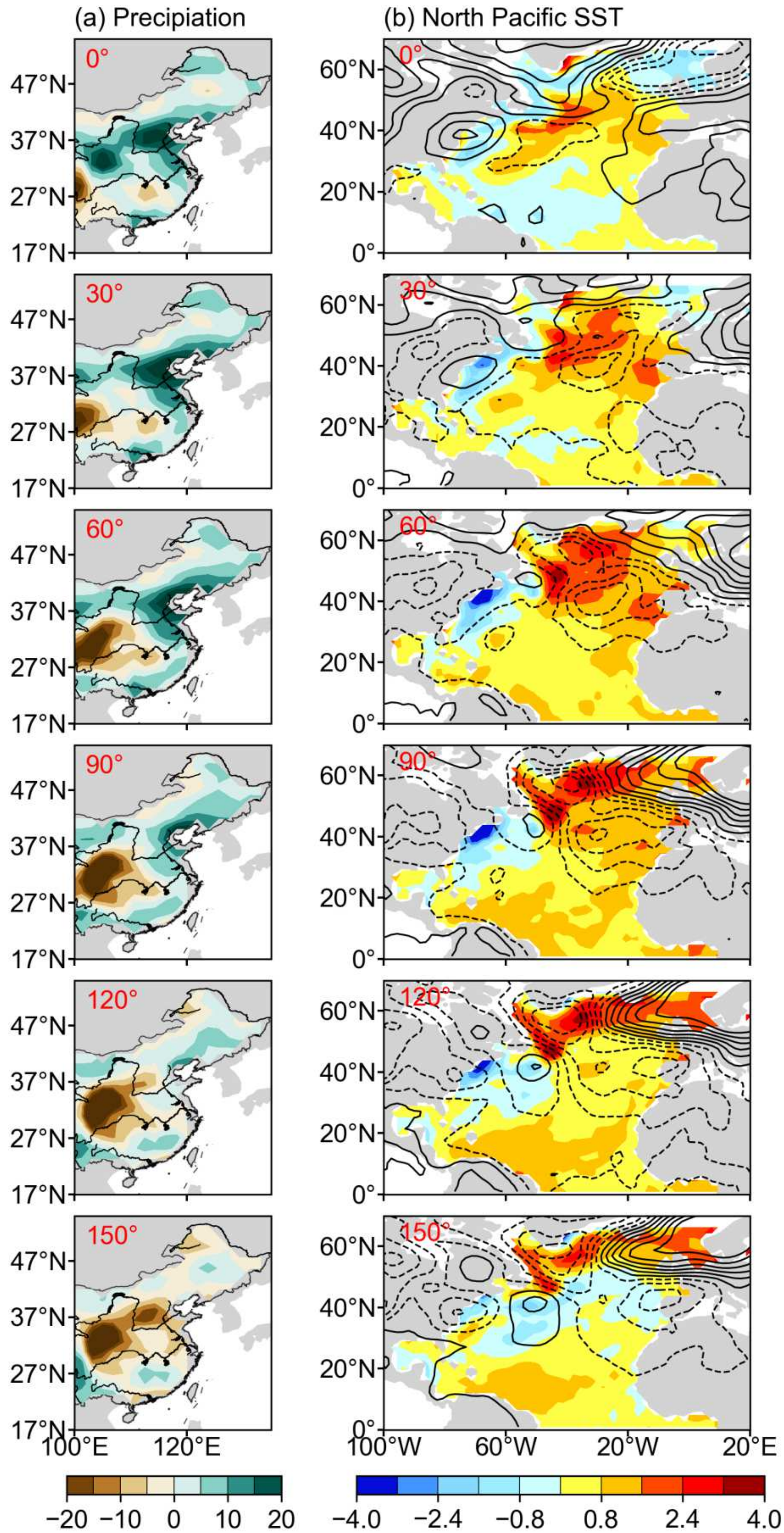

1041

1042 **Figure 9** Same as in Figure 4 but for the ATL experiment.

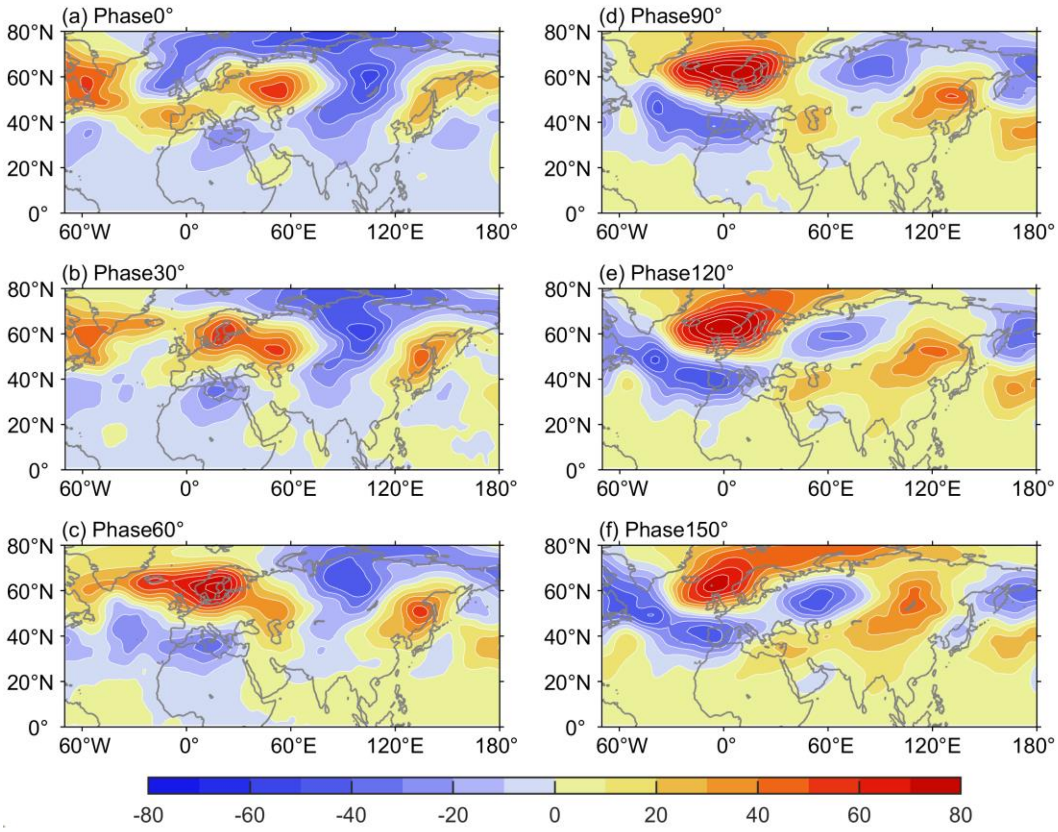

Figure 10. Same as in Figure 5 but from the North Atlantic to East Asia for the ATL experiment.

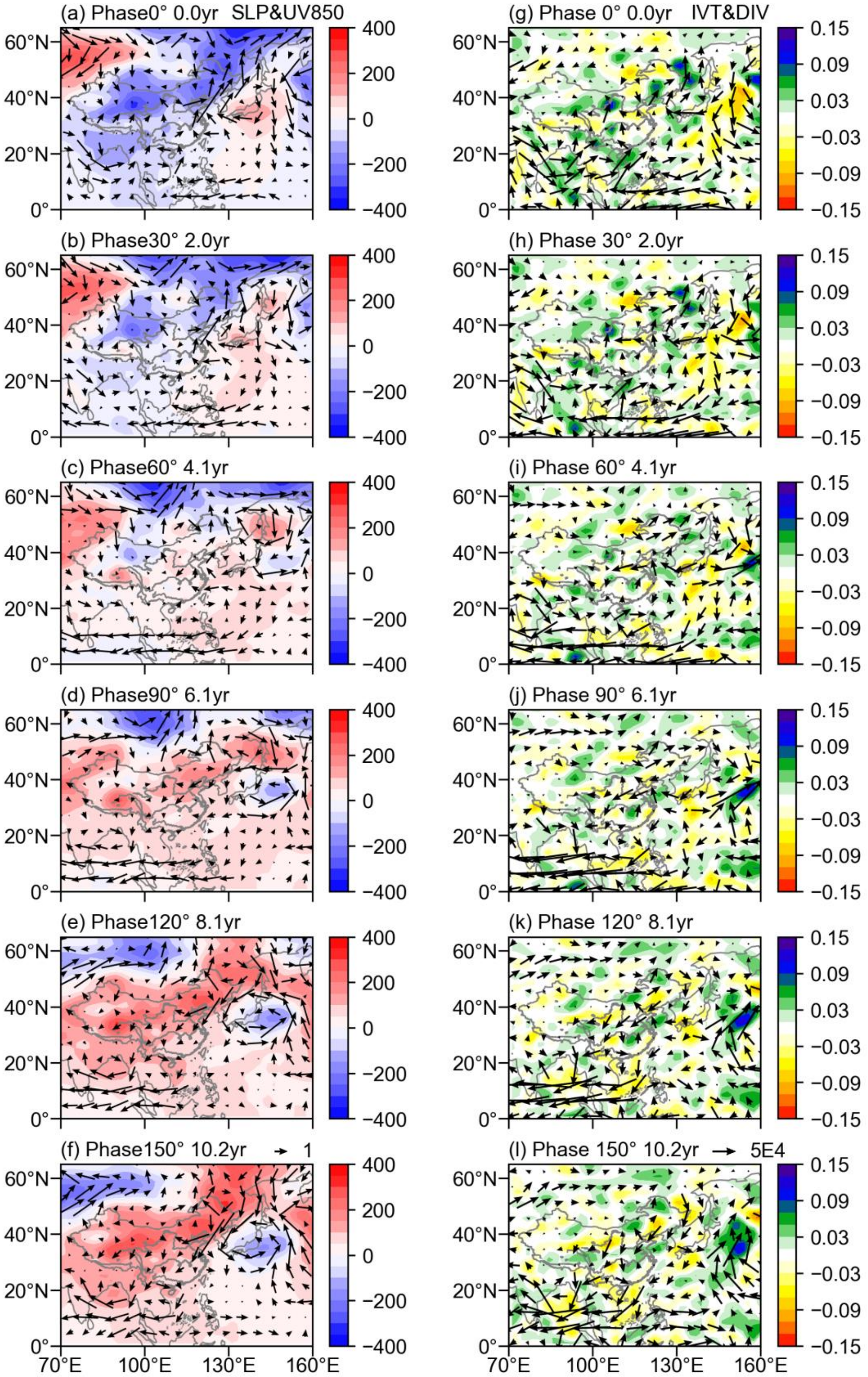

Figure 11 Same as in Figure 6 but for the ATL experiment.

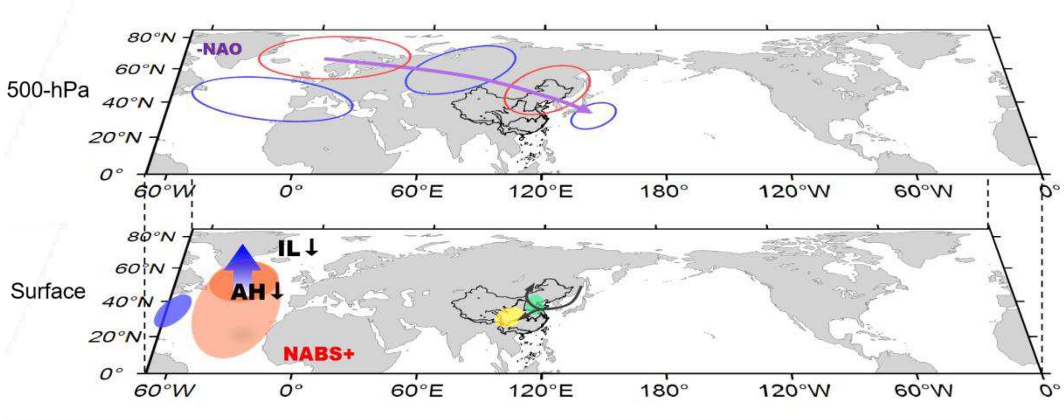

Figure 12. Schematic diagram showing the processes and mechanisms by which the North Atlantic SST anomalies affect the precipitation over eastern China during mature stages of the NABS+. At the surface (low panel), red/blue (green/yellow) shadings indicate positive/negative SST (precipitation) anomalies. At 500-hPa (top panel), red (blue) circles indicate anomalous anticyclonic (cyclonic) circulation. Black arrows indicate low-level winds, and blue broad arrows indicate ascending motions of the atmosphere.

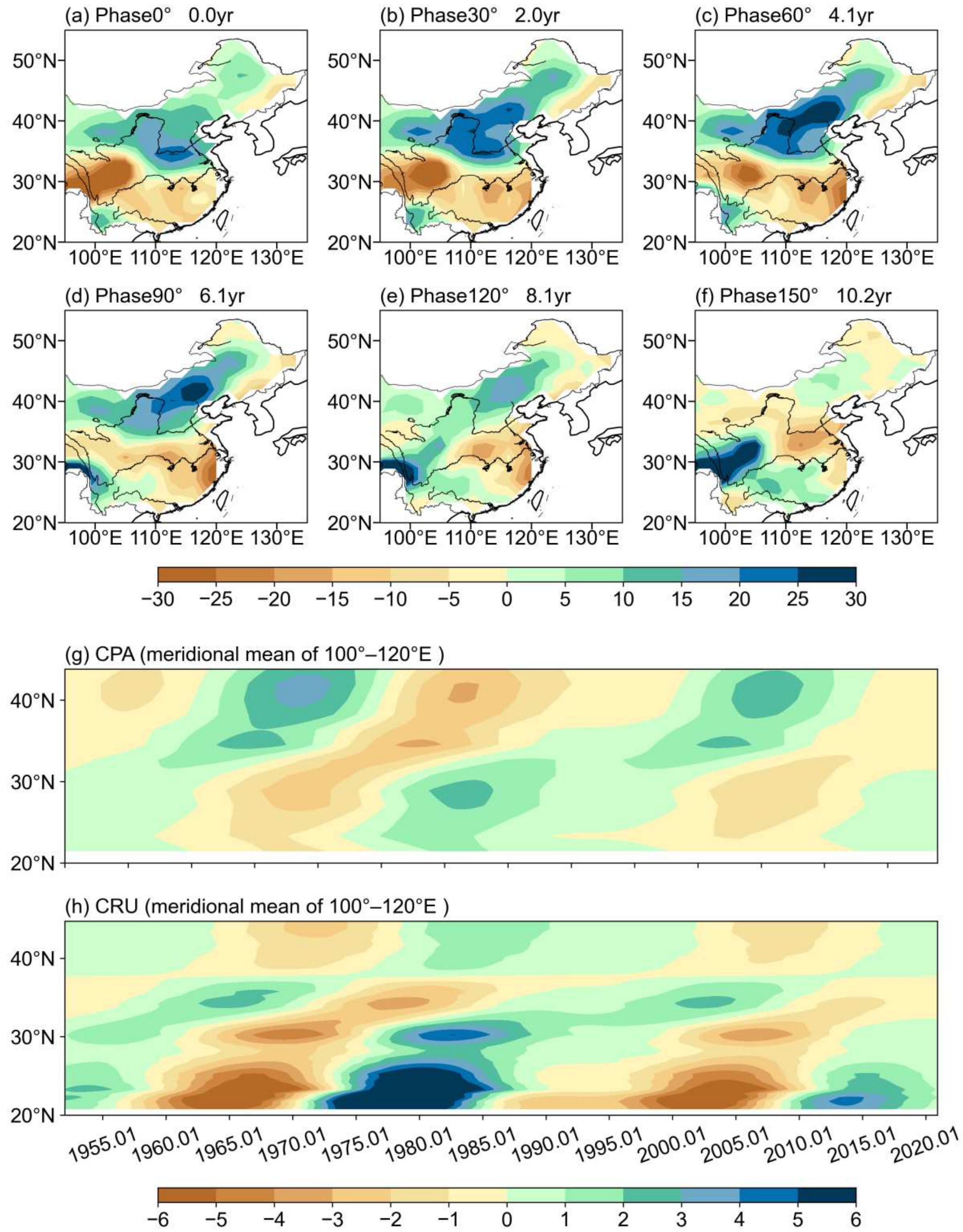

Figure 13. The half-cycle spatiotemporal evolution (a-f: Phases 0°–150°) of the (a) precipitation (mm mon^{-1}) over China. Time-latitude sections of meridional (100°–120°E) mean precipitation of the (g) CPA experiment and (h) CRU observation reconstructed at the 24-year cycle.

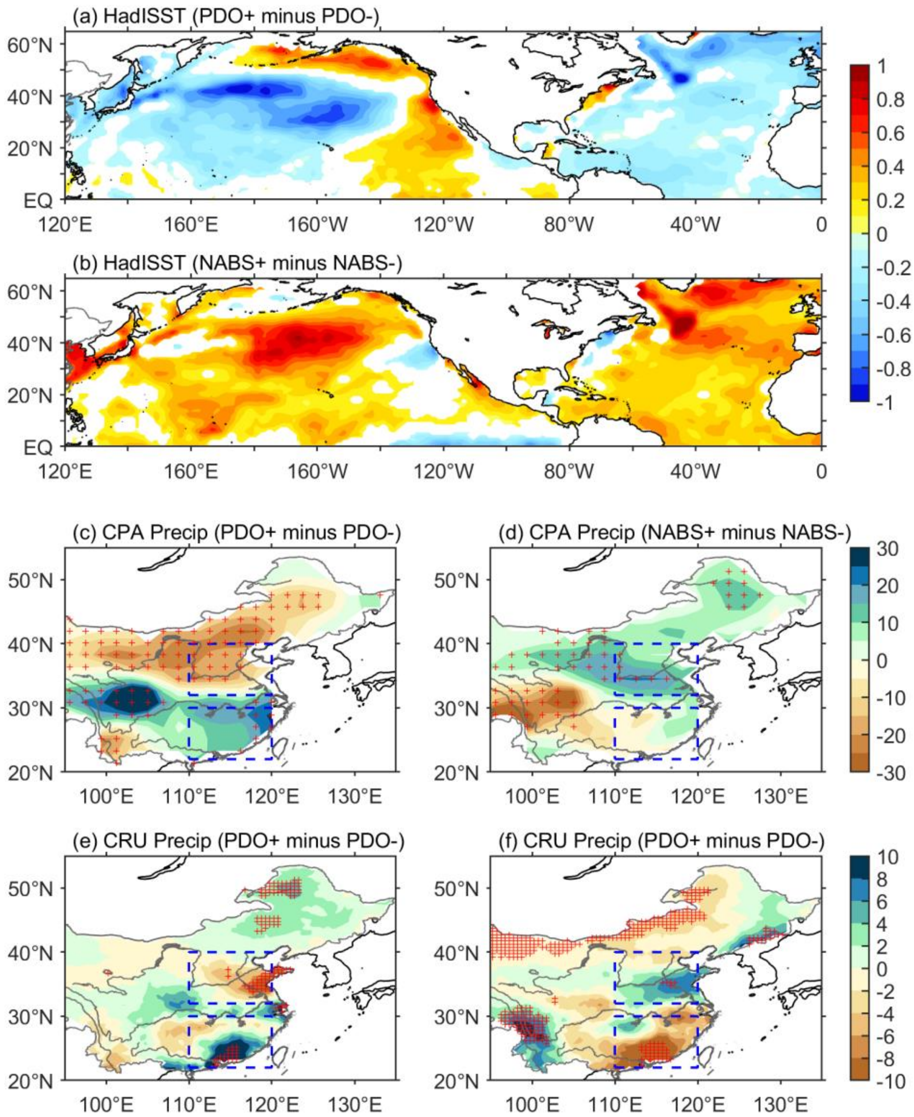

Figure 14. Composite analyses of the (a, b) SST and (c–f) precipitation over eastern China associated with the observations and CPA experiment: (a, c, e) PDO+ minus PDO− and (b, d, f) NABS+ minus NABS−. Only values at or above the 90% confidence level are shown in (a, b); the dots denote the regression values exceeding the 90% confidence level in (c–f). The blue boxes in (c–f) indicate in-phase precipitation variations between observations and CPA experiment in the corresponding regions.

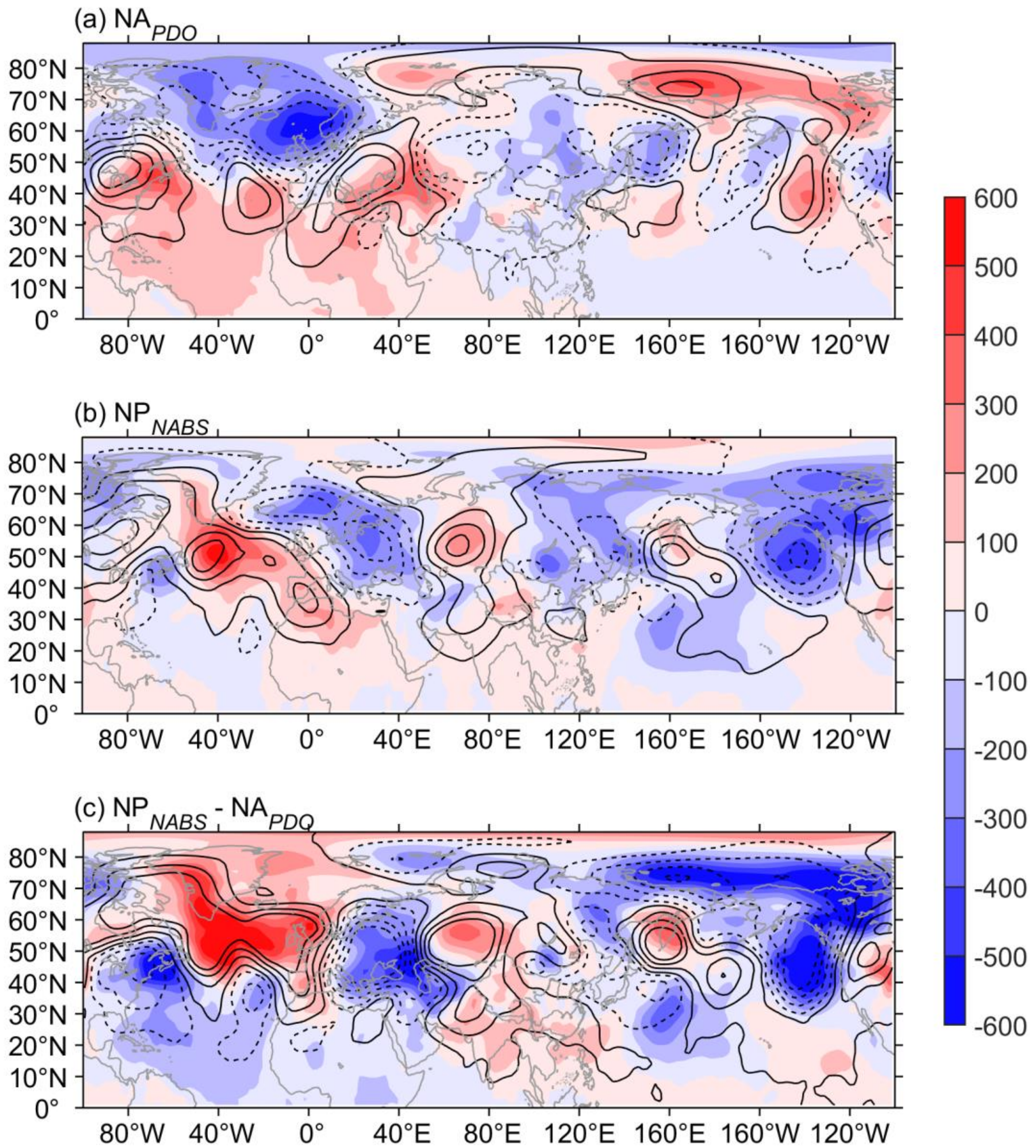

Figure 15. The SLP (shading; Pa) and 500-hPa GHT (contour; gpm) responses to the effects of SST: (a) NA$_{PDO}$, (b) NP$_{NABS}$, and (c) NP$_{NABS}$ minus NA$_{PDO}$. The contours are the ±5, ±20, ±35, ±50 gpm. The NA$_{PDO}$ (NP$_{NABS}$) is the composite analysis with respect to the PDO (NABS) phase based on the results of subtracting the PAC (ATL) experiment from the CPA experiment.

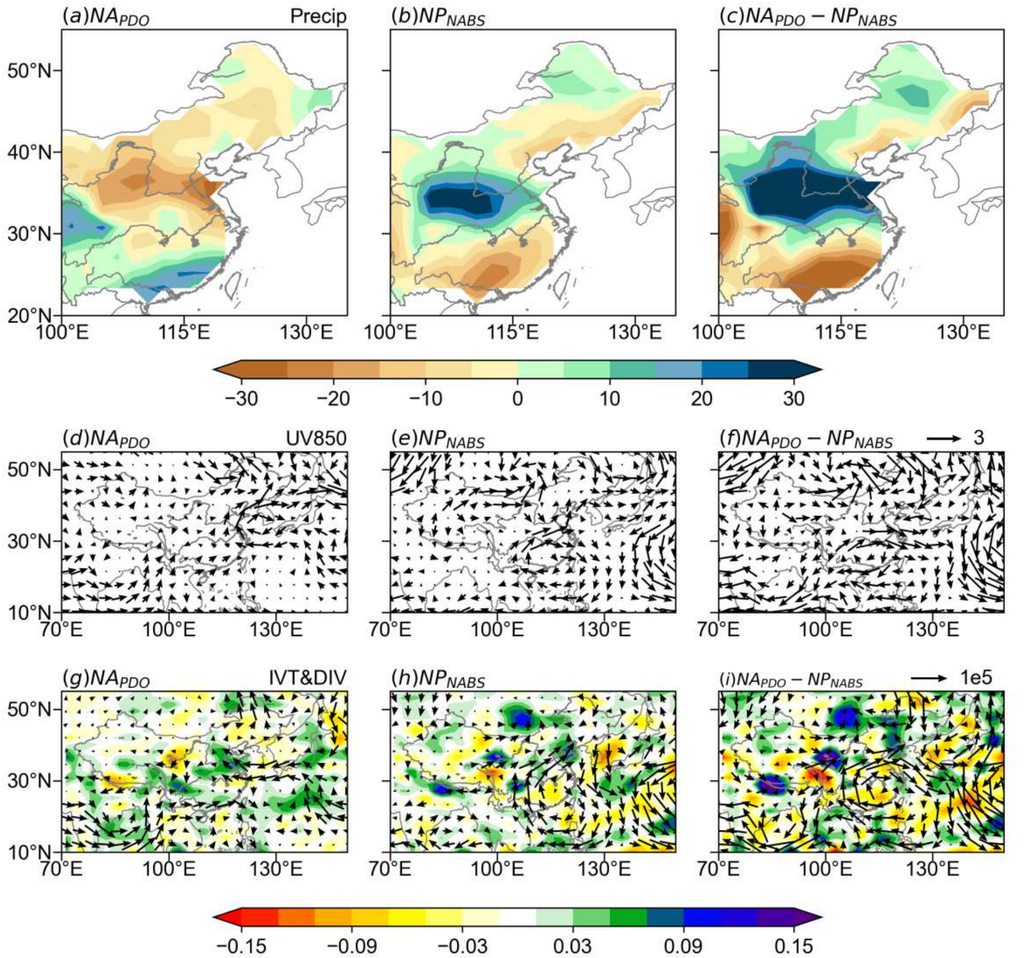

Figure 16. The atmospheric responses of the (a–c) precipitation (mm mon^{-1}), (d–f) 850-hPa winds (vector; m s^{-1}), and (g–i) vertically integrated water vapor flux (vector; g m^{-1} s^{-1}) and its divergence (shading; g m^{-2} s^{-1}) over East Asia to the North Atlantic SST forcing during the PDO+ (a, d, g; NA$_{PDO}$) and to the North Pacific SST forcing during NABS^{+} (b, e, h; NP$_{NABS}$). (c, f, i) are the differences between NP$_{NABS}$ and NA$_{PDO}$ in precipitation, 850-hPa winds, and water vapor flux.